Cytokine expression patterns predict suppression of vulnerable neural circuits in a mouse model of Alzheimer's disease

Dennis C. Chan[1,2,3,4,5], ChaeMin Kim[1,2], Rachel Y. Kang[1,2], Madison K. Kuhn[1,2,3,4], Lynne M. Beidler[1,2], Nanyin Zhang[3,4,5], Elizabeth A. Proctor[1,2,3,4,6]

1 Department of Neurosurgery, Penn State College of Medicine, Hershey, PA, USA
2 Department of Pharmacology, Penn State College of Medicine, Hershey, PA, USA
3 Department of Biomedical Engineering, Pennsylvania State University, University Park, PA, USA
4 Center for Neural Engineering, Pennsylvania State University, University Park, PA, USA
5 Center for Neurotechnology in Mental Health Research, Pennsylvania State University, University Park, PA, USA
6 Department of Engineering Science & Mechanics, Pennsylvania State University, University Park, PA, USA

Correspondence:
Elizabeth A. Proctor
500 University Dr, MC R130
Hershey, PA 17033
(717) 531-5922
eproctor@psu.edu

Abstract

Alzheimer's disease is a neurodegenerative disorder characterized by progressive amyloid plaque accumulation, tau tangle formation, neuroimmune dysregulation, synapse an neuron loss, and changes in neural circuit activation that lead to cognitive decline and dementia. Early molecular and cellular disease-instigating events occur 20 or more years prior to presentation of symptoms, making them difficult to study, and for many years amyloid-β, the aggregating peptide seeding amyloid plaques, was thought to be the toxic factor responsible for cognitive deficit. However, strategies targeting amyloid-β aggregation and deposition have largely failed to produce safe and effective therapies, and amyloid plaque levels poorly correlate with cognitive outcomes. However, a role still exists for amyloid-β in the variation in an individual's immune response to early, soluble forms of aggregates, and the downstream consequences of this immune response for aberrant cellular behaviors and creation of a detrimental tissue environment that harms neuron health and causes changes in neural circuit activation. Here, we perform functional magnetic resonance imaging of awake, unanesthetized Alzheimer's disease mice to map changes in functional connectivity over the course of disease progression, in comparison to wild-type littermates. In these same individual animals, we spatiotemporally profile the immune milieu by measuring cytokines, chemokines, and growth factors across various brain regions and over the course of disease progression from pre-pathology through established cognitive deficit. We identify specific signatures of immune activation predicting hyperactivity followed by suppression of intra- and then inter-regional functional connectivity in multiple disease-relevant brain regions, following the pattern of spread of amyloid pathology.

Introduction

13.8 million people are projected to be afflicted with Alzheimer's disease (AD) over the next couple decades (1,2, 3). It is a neurodegenerative condition characterized by an entanglement of disease pathologies, and cognitive impairment resulting in a decrease in quality of life (4, 5). Classical hallmarks of Alzheimer's Disease are the development and spread of neurotoxic amyloid-β peptides and oligomers (6-17) and neurofibrillary tau tangles (13-17) in parallel with neuroinflammation (15-20) and, ultimately, neuronal loss and brain tissue atrophy. The clinical symptomatic aspect of the described pathologies is the loss in cognitive performance, with cognitive impairment manifesting in spatial cognition, working memory and executive functions (16, 21). However, current treatment options for Alzheimer's Disease have failed to safely and meaningfully delay, slow, or halt disease, let alone reverse the effects on cognition (22, 23), potentially due to focus on single molecular targets. Integration of information from multiple aspects of AD pathology is likely needed to interrogate and correct the complex, systems-level mechanisms negatively impacting neuronal health, brain function, and cognition in AD.

One of the emerging biological factors of interest is the role that inflammation plays in the progression of Alzheimer's Disease. It has been detailed that neuroinflammation occurs over the progression of Alzheimer's Disease (15-20). On a more foundational level, it has been shown that neuroinflammation can have detrimental effects on neuronal behavior, such as predisposing neurons to be more sensitive to intrinsic excitability, resulting in increased rates of spontaneous action potentials, leading to an uncoordinated neuro-electrical behavior (27, 28). Moreover, cytokines have also been shown to have a profound effect on synaptic plasticity (28-30), demonstrating that microglia responses to adverse stimuli can affect neuronal behavior. Such effects can manifest in alterations to cognitive performance (28, 31), thus establishing a link between neuroinflammation and cognitive ability.

While the inflammatory environment is one neurophysiological event that influences cognitive behavior, another quintessential factor to driving cognitive performance is the level of neuronal activity (35, 36). This neurophysiological event can be described by brain regional activity and the regional combined behavior during a specific cognitive state. Thus, depending on the experimental paradigm, one can quantify how particular brain regions are involved at specific tasks (32-34), providing insight as to which region are involved in executing a particular task, quantifying what is called a functional network. While task based functional connectivity metrics yield insight into task specific networks, studies focusing on resting state functional connectivity (rsFC) have yielded a wealth of information as to how the brain organizes when no task is being performed (37, 38). It was found that such networks quantified during the resting state were different between comparing healthy controls to diseased populations or subjects afflicted with cognitive impairment (35, 36, 39-41).

Therefore, there is sufficient evidence that the regional inflammatory environment surrounding bodies of neurons can affect their behavior, and thus affect the spontaneous activations of brain regions that could influence cognitive behavior. However, the major limitation is that the majority of studies examining the above-mentioned factors study them in a univariate manner, excluding details how each individual factor affect each other over the progression of Alzheimer's Disease. Existing efforts to rectify the limitation includes the use deep learning or artificial intelligence to evaluate relationship cross-modality in large datasets (24-26). These datasets contain a wealth of information, and online databases such as the Alzheimer's Disease Neuroimaging Initiative (ADNI) offer a more comprehensive quantification of disease pathology. However, such datasets

lack spatial resolution when it comes to examining the inflammatory environment of individual brain regions, and only provide terminal data when quantifying the inflammatory environment of the brain. The consequence is that one can not determine how the development of Alzheimer's Disease can affect brain regions, thus driving changes to functional connectivity which then manifest as alterations to cognitive performance.

In our attempt to address the current limitation in the field, we describe an experiment that is centered around a well stereotyped mouse model of Alzheimer's Disease, and quantify the inflammatory environment of 3 cortical brain regions over four time points that are related to cumulative key events that occur during Alzheimer's Disease progression; before the development of disease pathology at month 1.5 (42), extracellular amyloid deposition occurring at month 2 (42, 43), deterioration of basal synaptic transmission in hippocampal CA1 at month 4 (42), and neuron loss at month 6 (42, 44-46). Additionally, we utilize awake resting state functional magnetic resonance imaging (rs-fMRI) to quantify the resting state functional connectivity during those four time points to correlate the functional connectivity to regional brain inflammation over disease progression. Our findings provide a new insight into how neuroinflammation and functional connectivity are intertwined in Alzheimer's Disease, thus highlighting which brain regions and networks are implicated in disease pathology at different stages of the neurodegenerative disease.

Methods

Animal subjects. Institutional and national guidelines for the care and use of laboratory animals were followed and approved by the Penn State Institutional Animal Care and Use Committee (PRAMS201647005). 5xFAD hemizygous B6SJL (MMRRC Strain #034840-JAX) background strain and wildtype mice were used to breed a colony of mice that were either hemizygous for the 5xFAD related genes, or wild-type littermates. All mice were genotyped following the protocol provided by Jackson Labs (Protocol Number: 31769). All mice were also genotyped for the retinal degenerative gene Pde6B using the protocol provided by Jackson Labs (Protocol Number: 31378). Animals that were found to be homozygous for the Pde6B gene were excluded from the study. Both male and female animals are included in the study. Mice were singly housed following headpost surgery (procedure below) at 1 month old. Food and water were provided *ad libitum.* Nesting material and chew blocks were provided to singly-housed mice as enrichment. The housing room was kept at 70 °C and adhered to a 12-hour light and 12-hour dark cycle. The study consisted of 160 mice: 27 for longitudinal imaging studies, 31 for age 1.5 months single timepoint, 33 for age 2 months single timepoint, 34 for age 4 months single timepoint, and 35 for age 6 months single timepoint. All mice underwent rs-fMRI. Cytokine protein levels were profiled in 105 animal brains from the same cohort of animals that underwent rs-fMRI: 25 mice for age 1.5 months, 26 for age 2 months, 27 for age 4 months, and 26 for age 6 months. All experiments were conducted during the 12-hour dark cycle to better capture the properties of the awake state, with euthanasia and tissue collection (procedure below)_directly following imaging. All experiments in the present study were approved by the Institutional Animal Care and Use Committee (IACUC) at the Pennsylvania State University.

Surgical Procedures. Mice had headpost implantation surgery done at 1 month old. Mice were anesthetized with 3% isoflurane and an oxygen flow of 1.0 L/min within an isoflurane chamber. The surgical plane of anesthesia was confirmed by pinching the lower limbs of the mouse, and if

no reaction was observed, the mouse was successfully anesthetized. The scalp of the mouse is then shaved using an electric clipper in preparation for surgery. A heating mat with a rectal probe (*PhysioSuite* with *RightTemp* from Kent Scientific) is used to maintain a body temperature around 36-37 degrees Celsius. A custom surgical setup that features the boundaries of the awake animal restrainer used in neuroimaging experiments is used. Once the mouse is in position, and the head is fixed for surgery, the scalp is cleaned twice alternating between provodine iodine and 70% isopropyl alcohol. Ophthalmic ointment is applied to the animal's eyes to prevent dryness during the course of surgery. The scalp is infiltrated with Bupivacaine (4mg/kg), followed by an anterior to posterior incision before excising the skin to form a circular excision anterior to the ears, and posterior to the eyes. All relevant soft tissue is then removed such as the periosteum, leaving only the skull exposed. The site is washed one time with sterilized saline solution. Once dried, an etching solution (composed of citric acid) is applied to the skull for 30 seconds before being rinsed off using saline solution. Dental cement (C&B Metabond) consisting of a ratio of 1 drop catalyst (C&B Metabond), 4 drops of "quick!" base (C&B Metabond), and 2 scoops of clear L powder (C&B Metabond) is applied to the exposed skull using a fine tipped brush. Rough edges are smoothed out during the process. Once set and cured, a custom head post constructed from polylactic acid (product number) is adhered to the dental cap using dental cement of the same recipe. Upon completion of procedure, meloxicam (5 mg/kg) is administered 2 days post-surgery. Weight and behavior in home cage is subsequently monitored for seven days where any weight drop lower than 20% of pre-surgical weight is recorded as a failure to recover from surgical procedure, and thus excluded from subsequent experiments. If weight and behavior is observed to be satisfactory (no weight loss, no abnormal behavior in home cage) for 4 consecutive days post-surgery, the mouse is then moved to subsequent experiments detailed below.

Acclimation Procedure. Mice were acclimated for awake animal imaging using a procedure adapted from an in-house pipeline. The mice were habituated to the restrainer used for imaging where the process lasted 4 days prior to the imaging experiment. An acclimation box was used alongside custom made holders that mimic the interior of a scanner. All mice were first anesthetized using 3% isoflurane, and an oxygen flow of 1.0 L/min. Once anesthetized, mice had their front limbs bounded together using tape before restraining the mice by attaching a custom-made head bar that connected the implanted headpost to the custom-made restrainer. Once the animals were confirmed to be awake, they were given five minutes to adjust to being restrained before the acclimation process started. The first day of acclimation was 15 minutes with no sound. The second, third and fourth day of acclimation was 30 minutes, 45 minutes, and 60 minutes respectively. A soundtrack that had the recording of the noise heard during an fMRI session was played for the stated durations at the second, third and fourth day at 110 db. Once acclimation was over, the mice were anesthetized before being removed from the restrainer, and then placed back into their home cage. Weights before and after restraining were recorded, alongside any behavioral abnormalities such as tears forming.

fMRI Imaging. Awake resting state imaging was conducted on a 7T MRI system interfaced with a Bruker Console (Billerica, MA) housed at the High Field MRI Facility at Pennsylvania State University, University Park. Gradient Echo images were acquired using an echo-planar imaging (EPI) sequence with the following parameters: repetition time (TR) of 1.5 second, echo time (TE) of 15 milliseconds, flip angle = 60°, matrix size = 64 x 64, FOV = 1.6 x 1.6 cm^2 number of slices = 16, slice dimensions = 0.25 mm x 0.25 mm x 0.75 mm. 10 or 32 dummy scans were taken before each EPI acquisition. A trigger delay of 10 milliseconds was set at the beginning of each volume acquisition such that real time monitoring of respiration rate can be synchronized to the volume

acquisition. Respiration was monitored using a custom-made nose cone perforated with angled holes to allow carbon dioxide to diffuse out and oxygen to diffuse in without significant loss of pressure. The respiration monitoring system was connected to the 7T MRI system using a MR-compatible monitoring and gating system (Model 1030 from Small Animal Instruments Inc.), which was also interfaced with a desktop that housed the respiration monitoring software from Small Animal Instruments Inc. A total of 4 or 5 EPI scans were collected for every imaging session.

Following the completion of EPI acquisition, a structural T1 RARE image was collected. The imaging parameters are as follows: repetition time (TR) of 1500 seconds, echo time (TE) of 8 milliseconds, flip angle = 90°, matrix size = 256 x 256, FOV = 1.6 x 1.6 cm^2 number of slices = 16, slice dimensions = 0.25 mm x 0.25 mm x 0.75 mm.

fMRI Image Preprocessing. fMRI images and the corresponding T1RARE structural images were preprocessed following a paradigm adapted from an in-house pipeline (47, 48). All processes and scripts described in this section were done using MATLAB 2022b. Briefly described, EPI time courses were first converted from the standard Bruker file format to a .sdt file format before undergoing motion scrubbing. The following formula was used to determine the degree of motion for an isotropic shape:

$$\text{Motion Parameter} = |T_z| + |T_y| + |T_x| + |\theta_x r_z| + |\theta_y r_z| + |\theta_z r_x|$$

Euler angles were back computed from the affine transformation matrix calculated using an internal MATLAB function. Volumes that exceeded half a voxel size of displacement (0.125 mm) were discarded, along with one volume preceding it, and one volume after the volume exhibiting excessive motion. Scans that had more than 10% of volumes discarded due to motion (including the number of neighboring volumes) were discarded. Thus, scans with at least 90% remaining volumes post motion scrubbing were kept for following preprocessing.

Post motion scrubbing, each scan will undergo the process of co-registration and normalization. First, the first frame for each EPI scan is co registered to the relevant subject's T1RARE structural image using an in-house GUI made in MATLAB. Following co-registration, the subjects T1RARE image is then normalized to a reference brain atlas from the Allen Brain Atlas (WEBSITE). After successful normalization, the affine transformation matrix from the normalization process is then applied to the co-registered EPI images to align the EPI images to the reference brain atlas. Once the first frame for every EPI scan has been successfully aligned to the reference template following the beforementioned procedure, the scans are then motion corrected using functions from Statistical Parametric Mapping (SPM12, 49). Post motion correction, a custom mask for every EPI scan was manually drawn using the first frame for every motion corrected scan. The custom mask excludes areas with significant signal distortion, and is subsequently applied to the postprocessing step. White matter and cerebral spinal fluid (WM-CSF) masks are constructed using the reference atlas to determine the spatial location of the specified features. The signal in the WM-CSF mask is then used as a nuisance regressor alongside the motion parameters calculated from motion correction using SPM12 in a general linear model. The residuals from the general linear model is then spatially smoothed using a 3x3 Gaussian kernel, followed by temporal filtering using a bandpass filter with a cutoff frequency of 0.01 Hz and 0.1 Hz. The end result is a correlation matrix consisting of pairwise correlations between each ROI in the mouse's brain.

fMRI Image Postprocessing. fMRI ROIs were grouped into seven anatomical systems for system ROI analysis. These seven systems were the Sensorimotor Cortex, Heteromodal Cortex, Olfactory Cortex, Hippocampus, Striatum-Pallidum, Thalamus, and Hypothalamus. System representative functional connectivity values are calculated as the mean correlation value where

all related ROIs correlation values first undergo fisher Z transformation from r space to z space, before calculating the mean, and then back transformed into r space. The process is repeated for every scan within a group, and the group average are also quantified in the same manner.

The initial evaluation of the entire dataset comprised of examining the correlation matrices in a univariate manner, where every pairwise functional connectivity value is fisher-z transformed (using the arctanh function), followed by implementing a linear mixed effect model of the following structure:

$$y = X\beta + Zu + \varepsilon$$

Where y is the response vector with n x 1 dimensions, n being the number of subjects. X is defined as the predictor matrix, with n x p dimensions, where p is the number of fixed effect predictors (dependent on analysis), β is the p x 1 vector of fixed effect coefficients. Z is a n x $q \cdot m$ matrix where there are q random effects and m groups. u is defined as a random vector with dimensions $q \cdot m$ x 1 for m groups. ε is the residual vector for n groups. The random effects are the subjects While the fixed effects are some combination of genotype and timepoint, dependent on the statistical question being evaluated (e.g. time point segregated data will only have genotype as the fixed effect to evaluate differences at a single time point). A two-way ANOVA or two-tailed t-test (depending on the model) is conducted to evaluate the statistical significance of the coefficients derived from the linear mixed effect model.

Anatomical System definitions. Anatomical systems such as the Sensorimotor Cortex, Heteromodal Cortex, Olfactory Cortex, Hippocampal Region, Basal Ganglia, Thalamus, Hypothalamus consists of sub ROIs featured in the respective systems. The quantification of the inter and intra system connectivity is achieved by calculating the mean of the fisher z's transformed correlation values of all ROIs within a system-system interaction. For example, if we are to calculate the system connectivity between the Hippocampal region and the Heteromodal Cortex, then all functional connectivity values between the ROIs within both systems are averaged following the steps described previously. The system definitions for each individual ROI is listed in a table in the supplementary materials.

Brain Extraction. Mice were euthanized via decapitation by placing the awake mouse into a decapicone and using a guillotine. The decapitated head was then sprayed with 70% sterile ethanol. The skin and muscle are removed from the skull by removing the skin surrounding the cement cap. Forceps are used to grasp the head post attachment and apply a measured amount of force to slowly rock the dental cap back and forth to slowly loosen the cement cap from the skull. Once the cement cap is 'peeled' off from the skull, dissection scissors are used to cut up the side of the spinal cord and around the base of the skull at the lateral and ventral borders. The scissors are then inserted at the base of the skull and are used to make a cut down the midline of the skull from posterior to anterior direction. The dorsal part of the skull is then removed and the brain is slowly and carefully dislodged and placed in a separate cell culture dish containing chilled dissection media (x mL of HBSS and x/90 mL 1 M HEPES) hosted within a bed of ice and placed on top of a chilled copper plate.

The brain is then halved into two separate hemispheres, with the right hemisphere to be dissected into individual brain regions. The brain regions are the Cerebellum, Hypothalamus, Thalamus, Striatum, Hippocampus, Occipital Lobe, Temporal Lobe, Parietal Lobe, and Frontal Lobe. Each individual brain region is placed into their own respective centrifuge tubes that holds a mixture of lysis buffer and protease inhibitor. The brain regions are homogenized by mechanical titration before sitting for 20 minutes on ice before being centrifuged at 5000 rpm for 5 minutes at 4

degrees Celsius. The supernatant is then placed into a separate tube, and flash frozen in liquid nitrogen and stored at a -80 degrees Celsius freezer until further use.

Quantification of protein. Total protein content in the supernatant was quantified using the Pierce BCA Protein Assay kit (Fisher 23225). Manufacturer's instructions were followed accordingly. Samples were run using technical duplicates and absorbance was quantified using a *SpectraMax* i3 minimax 300 imaging cytometer (Molecular Devices). Linear regression was used to quantify protein concentration.

Multiplex Assay. Cytokine concentrations of dissected homogenized brain regions from 5xFAD mice were quantified using the Bio-Plex Pro Mouse Cytokines Grp1 Panel 23 Plex (Cat. #M60009RDPD) using the Luminex FLEXMAP3D platform. Manufacturer's protocol was performed with minor modifications to accommodate the use of a 384 well plate. Following steps are applied using existing in-lab protocols (58). Streptavidin-phycoerythin was used at half volume While magnetic beads and antibody solutions were diluted 1:1 and used at half volume. Equal parts of lysis buffer lysis assay buffer were used in the preparation of standards and blanks.

Cytokine Data Cleaning. The Xponent software provided by the Luminex System was used to interpolate sample cytokine concentrations using standard curves derived from using the 5 point logistic regression model. Concentrations below or above the standard limit are either set to 0 pg/mL or the maximum concentration on the curve respectively. An in-house pipeline was used to clean the cytokine data (64): https://github.com/elizabethproctor/Luminex-Data-Cleaning (version 1.05). All cytokines with above-background values for at least half of the subjects were used in further analysis of the cytokine data; we included cytokines with fewer non-zero values if the non-zeros appeared biased toward a particular group.

Partial Least Squares Modeling. We utilized a linear, supervised multivariate regression model known as Partial Least Squares (PLS) (61,62) to model Cytokine Signatures of disease and healthy control states. The ROPLS package in R (63) was used to run both Partial Least Squares Regression (PLSR), and Partial Least Squares Discriminant Analysis (PLS-DA). PLSR was used to construct a predictive model to model a continuous response variable, such as the timepoint of our covariates. PLS-DA was used to create a classification model that sought to discriminate disease from healthy control cytokine signature profiles. All cytokine data was z scored to mean center the data and have the sample distribution exhibit unit variance.

Random sub sampling cross validation tests were conducted to select the appropriate number of latent variables (LVs) for both PLSR and PLS-DA models. Test sets and training sets were determined by randomly sampling the parent dataset. The number of k-folds, consequentially determining the size of the training and test sets, was determined by the following criteria (64): k -Folds = 3 if the number of samples exceeded 30, or k-folds = 5 if the number of samples building model was less than 30. K-fold cross validation was conducted a hundred times. 3 models consisting of either 1, 2, or 3 LVs were constructed in every iteration of the Cross-Validation process. All models were then used to predict the response variable, or class identity to quantify the prediction accuracy for PLS-DA, or the root mean squared error of cross validation (RMSECV) for PLSR. RMSECV has the following formulae:

$$\mathrm{RMSECV} = \sqrt{\frac{\sum_{j=1}^{n}(x_j - \hat{x}_j)^2}{n}}$$

Where x_j is the predicted value for the jth sample, $\hat{x}_j$ is the actual value for the jth sample, and n is the number of samples in the test set. Every iteration resulted in a completely new random sampling of the parent dataset to produce both the test and training datasets for cross validation. The number of LVs was determined by selecting the models, and their number of LVs that they represented, that had the lowest RMSECV, or highest predictive accuracy. This model is then used for subsequent analysis and significance testing.

Significance testing of the model was conducted by permutation testing. 1000 permutations were done to construct a null distribution of random models, where each iteration involved the scrambling of the response variable of interest with respect to the covariates. The final model's predictive accuracy or RMSERCV is then used to calculate a z score:

$$Z = \frac{x_{\text{Model}} - \mu_{\text{Null}}}{\sigma_{\text{Null}}}$$

Where x_{Model} is the model's predictive accuracy or RMSECV, and μ_{Null} is the mean predictive/RMSERCV of the null distribution, and σ_{Null} is the standard deviation of the null distribution simulated by the permutation process. We then calculate the corresponding p value for the significance of the model by comparing the calculated Z score to the Z distribution.

Models that were determined to only have one latent variable will have score plots that show two latent variables for ease of visualization. However, only the one latent variable model is used to inspect the loadings, and to make interpretations about the cytokine profile with relation to disease state. The models here are also orthogonalized for improved interpretability. The orthogonalization process results in projecting the maximal amount of covariance in the response vector and the covariate matrix onto the first latent variable (65). The variable importance in projection (VIP) score was used to threshold which cytokines drove the separation between classes with respect to the response of interest (66). Thus, loadings from the first latent variable for cytokines that had a VIP score greater than 1 are designated as cytokines of interest, as they are implied to have a greater than average contribution to the model.

Graph Theoretical analysis. Every functional connectivity matrix (the preprocessed correlation matrix) is converted into a weighted adjacency matrix where the absolute value of the correlation values is used as the weights of each edge. All graph organizational metrics were calculated using the Brain Connectivity Toolbox (50). Hub regions were identified by allocating a score of 0-4 based on the following criteria: 20% highest strength, 20% highest betweenness centrality, 20% lowest path length, and 20% lowest clustering coefficient (51). The graph theory metrics used to determine the hub score were quantified on the group average correlation matrix for every group. The mathematical definitions for the four topological features are described below:

Strength (50, 52):

$$\mathrm{S}_i = \sum_{j \in N} w_{ij}$$

Where S_i is defined as the strength for the ith node. $W_{I,j}$ is defined as the weight of the edge between node i and its jth neighbor, and N is the set of all nodes. Strength quantifies the degree of connection between a node and its neighbors.

Clustering Coefficient (50, 53):

$$C_i = \frac{1}{k_i(k_i - 1)} \sum_{j,k \in N} (w_{i,j} w_{j,k} w_{k,i})^{1/3}$$

$W_{i,j}$ is the weight between node i and node j, and k_i is the number of neighbors of a vertex. The clustering coefficient can be interpreted as the degree to which nodes tend to cluster together. For the local clustering coefficient, C_i, the coefficient quantifies how close the neighbors are to node i to being a clique. N is the set of all nodes.

Characteristic Path length (50, 55):

$$L^w = \frac{1}{n}\sum_{i\in N}\frac{\sum_{j\in N, i\neq j} d_{ij}^w}{n-1}$$

N is the set of all nodes, n is the total number of nodes, and d_{ij}^w is the weighted shortest path between nodes i and j. Characteristic path length quantifies the proximity with regards to strength of connection between nodes.

Global Efficiency (50, 56):

$$E^w = \frac{1}{n}\sum_{i\in N}\frac{\sum_{j\in N, i\neq j} d_{ij}^{w^{-1}}}{n-1}$$

N is the set of all nodes, n is the total number of nodes, and d_{ij}^w is the weighted shortest path between nodes i and j. Efficiency is essentially the mean of all reciprocals of the weighted distances in a network. The metric quantifies how efficient information is exchanged within a network.

Assortativity (50, 57):

$$r^w = \frac{l^{-1}\sum_{(i,j)\in L} w_{ij}k_i^w k_j^w - [l^{-1}\sum_{(i,j)\in L}\frac{1}{2}w_{ij}(k_i^w + k_j^w)]^2}{l^{-1}\sum_{(i,j)\in L}\frac{1}{2}w_{ij}(k_i^{w^2} + k_j^{w^2}) - [l^{-1}\sum_{(i,j)\in L}\frac{1}{2}w_{ij}(k_i^w + k_j^w)]^2}$$

Where k_i^w and k_j^w are the weighted degrees of nodes i and j. w_{ij} is the weight of the edge between nodes i and j, l is the total number of edges, While L is the set of all edges within the network. Assortativity is used to determine the degree to which nodes connect to other nodes with similar properties within the network.

Results

Hippocampal functional connectivity exhibits local suppression before propagating to inter- and intra-regional connectivity loss in thalamus and cortical regions. To investigate the effects of Alzheimer's Disease progression on functional networks, we quantified functional connectivity matrices at four different time points: month 1.5, month 2, month 4 and month 6; utilizing our awake resting state animal imaging paradigm. What we initially observed was that the majority of pairwise ROIs exhibited a time effect, but not an interaction between genotype and time (**Figure 1A**). We noticed that when examining the connectivity values at each timepoint, the values diverged at later time points, but were parallel to each other at the earlier stages of disease development (**Figure 1B**), with the divergence in connectivity is markedly shown at the latest stage of disease development, but not exhibited in the other three timepoints. Thus, we proceeded to investigate differences between disease and wildtype mice at each particular timepoint, acting on the assumption that the differences in connectivity values did not follow a linear pattern. The connectivity values were found to be statistically different between disease and control ($p < 0.05$, uncorrected for multiple comparisons) vary when transitioning from consecutive timepoints and

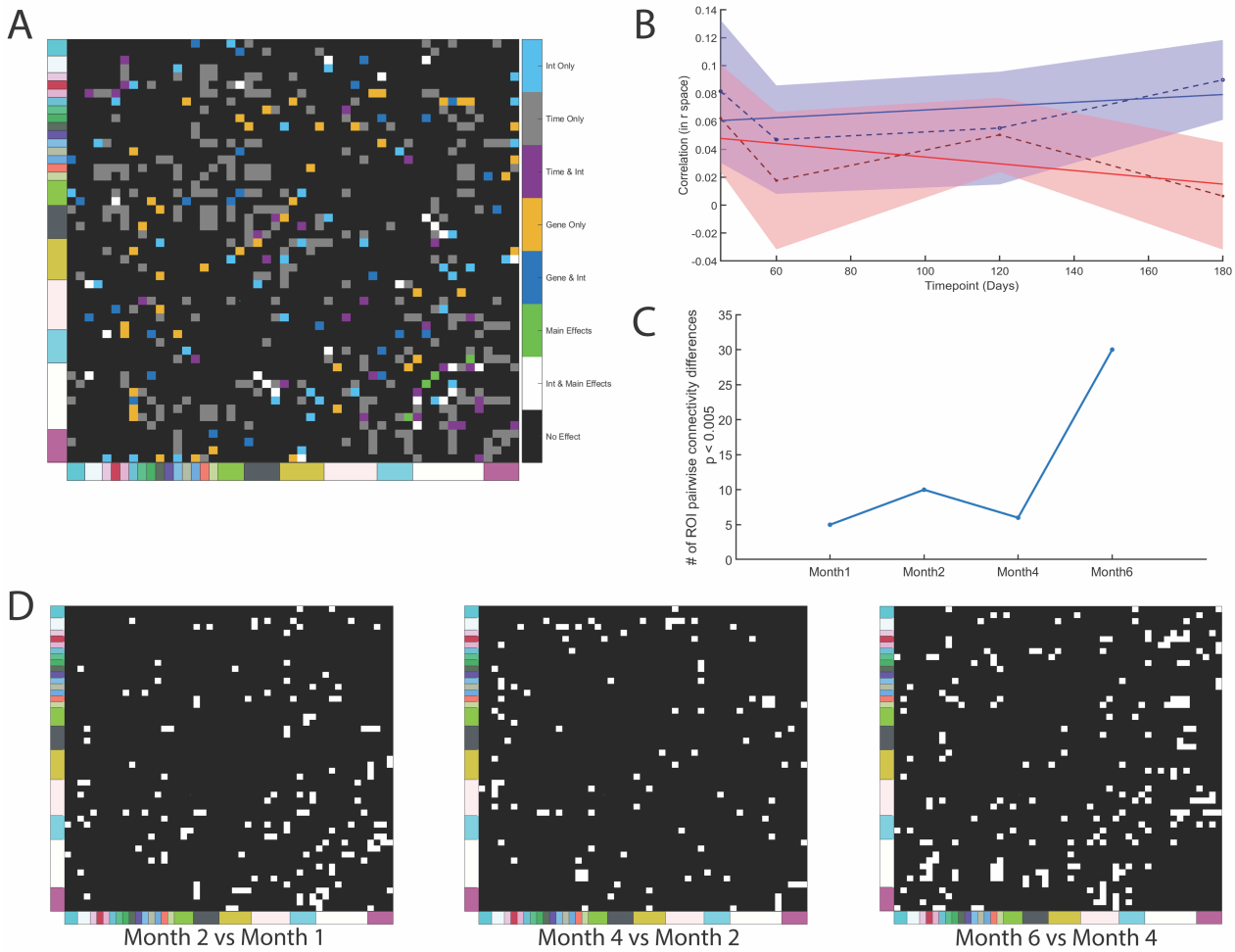

Figure 1. Disease-relevant changes in connectivity of anatomically defined ROIs accumulate non-linearly over time. A) Color-coded binary plot illustrating which connections between ROIs exhibit a disease effect (linear mixed effect model, disease and time as fixed effects, subject as random effect). Interaction term is included. B) Representative time-course ROI-ROI functional connectivity (Postsubiculum and Taenia Tecta), where mean response is plotted with 95% CI. C) Number of ROI-ROI functional connections significantly changed in disease vs. wild-type at each time point, one-tailed t-test with cutoff $p < 0.005$. D) Binary masks identifying ROI-ROI functional connections significantly changed in disease vs. wild-type at each time point, one tailed t-test with cutoff $p < 0.05$.

modeling pairwise ROI differences between them for both 5xFAD and wildtype mice in a two way ANOVA model (**Figure 1C,D**).

When examining the difference in the global network at each timepoint, we note a couple distinct features of the difference matrices. At month 4 we observe a distinct local depression of functional connectivity in ROIs located in the hippocampal region, and that at month 6 there is a significant increase in the number of pairwise ROI connectivity relationships that are different between the disease and control groups (**Figure 2**). The observation is further confirmed when examining the binary matrix which highlights regions that exhibited a statistically significant difference ($p < 0.05$, uncorrected) between the disease and control group. It can be seen that hippocampal ROIs such as the Subiculum, Presubiculum, Field CA1, Field CA2, Dentate Gyrus (DG) and the Entorhinal area exhibit significantly depressed intra-regional connectivity ($p_{\text{Presubiculum-Field CA2}} = 0.0031$, $p_{\text{Presubiculum-Field CA1}} = 0.015$, $p_{\text{Field CA3-Field CA2}} = 0.029$, $p_{\text{Presubiculum-DG}} = 0.041$, $p_{\text{Subiculum-DG}} = 0.041$, $p_{\text{Subiculum-Presubiculum}} = 0.041$, $p_{\text{Presubiculum-Entorhinal area}} = 0.046$) at month 4 for the disease group. Some

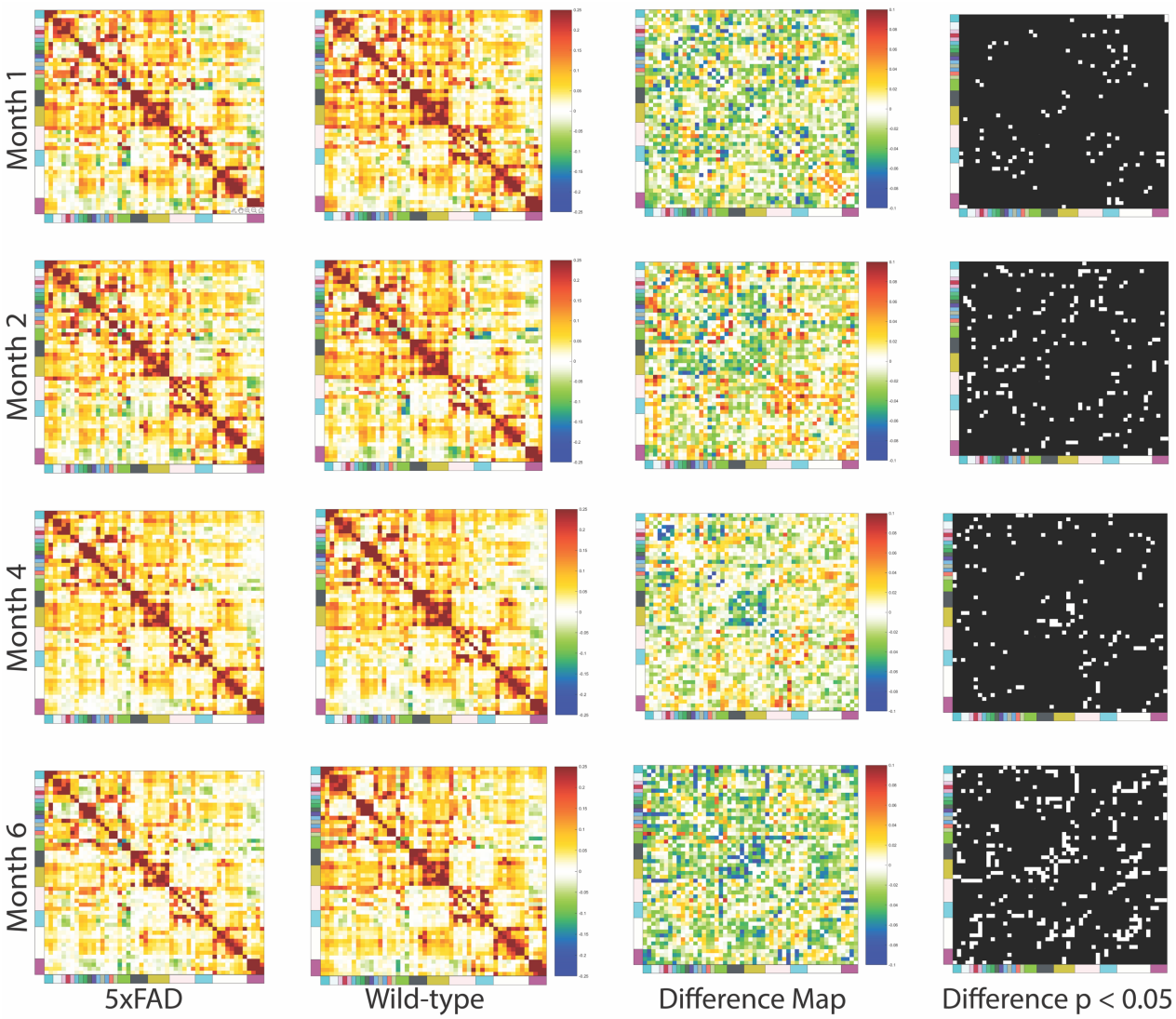

Figure 2. Functional connectivity changes over the course of AD and healthy aging. Symmetric heat maps of Pearson's correlation coefficients between brain regions of interest. Left to right, column 1: 5xFAD transgenic Alzheimer's disease mice at age 1.5, 2, 4, or 6 months (rows 1-4, respectively). Column 2: wild-type littermates at the same ages. Column 3: difference matrix representing the changes due to disease (5xFAD minus WT, Z-transformed subtraction). Column 4: binary matrix highlighting connectivity values with two-tailed t test $p < 0.05$ of LME fixed effect coefficients.

of them such as the retrohippocampal ROIs exhibit lower intra-ROI connectivity While the hippocampal formation ROIs displayed lower inter-ROI connectivity with retrohippocampal regions such as the Presubiculum.

Another feature that we observe is the level of thalamic ROIs that exhibit differences between the two groups at each specific timepoint markedly increases at month 6. Both inter and intra region connectivity for the Thalamus was depressed at the fully symptomatic timepoint (**Figure 2**). One interesting result is that the 5xFAD group exhibited a higher level of thalamus to Pallidum connectivity relative to the wildtype group at month 2, where both the Globus Pallidus and the Substantia innominate displayed stronger connectivity with subregions in the dorsal Thalamus ($p_{\text{Midline group of the dorsal thalamus-Globus pallidus}} = 0.038$, $p_{\text{Midline group of the dorsal thalamus-Substantia innominate}} = 0.036$, $p_{\text{Reticular nucleus of the thalamus-Striatum-like amygdalar nuclei}} = 0.028$) . This particular feature is lost at month 4, and instead we note that inter-striatum-thalamic connectivity and inter striatum-hypothalamic

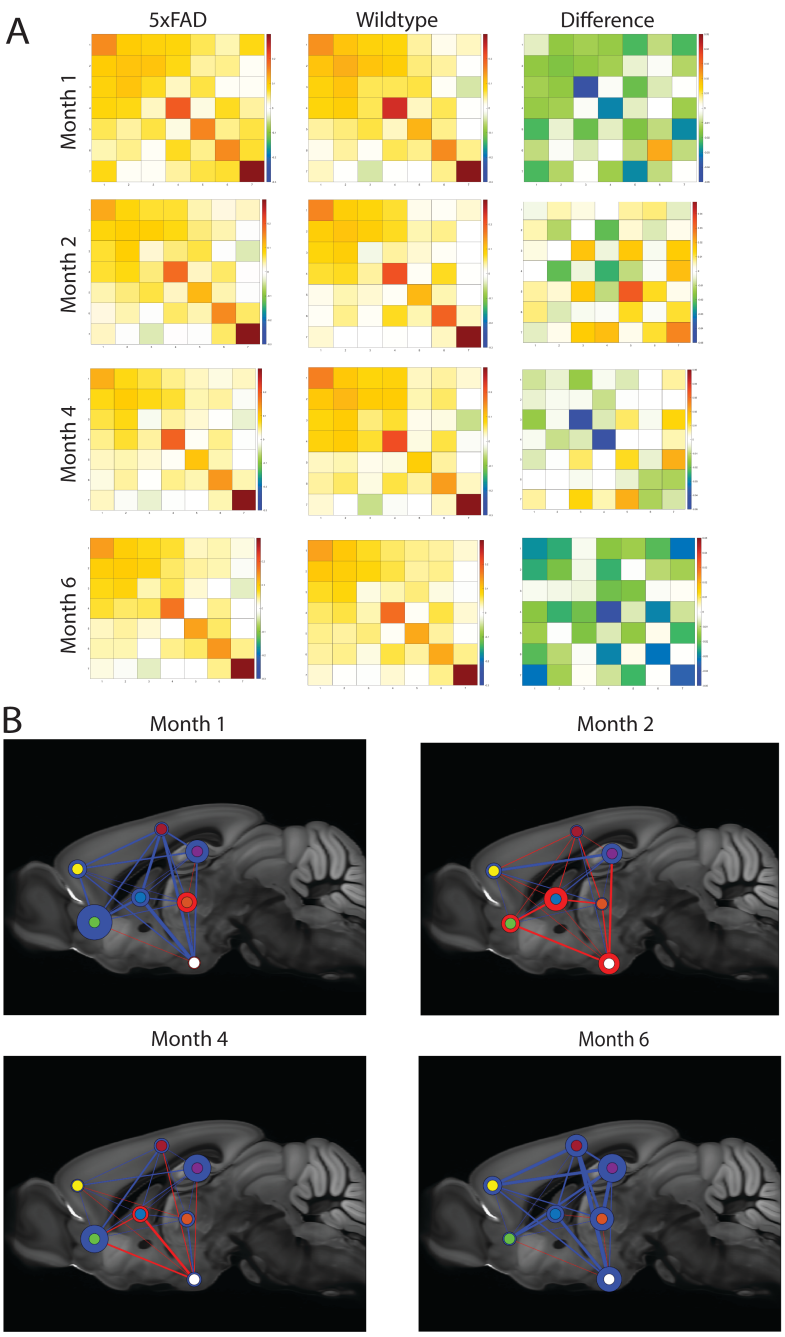

Figure 3. Brain anatomical systems exhibit hyperconnectivity followed by suppression in an AD-relevant spatiotemporal pattern. A) Connectivity matrices and the difference matrix at each respective timepoint, as in Figure 2. B) Spatial illustration of difference matrix in a binarized form superimposed over an anatomical brain slice. Blue: negative change in connectivity, Red: positive change in connectivity. Thicker edges have higher magnitude of change. Color of node outline indicates directionality of intra-system connectivity changes, with greater outline thickness indicating greater magnitude of intra-region connectivity change. Node color: yellow = sensorimotor cortex, red = heteromodal cortex, purple = hippocampus, blue = basal ganglia, orange = thalamus, green = olfactory cortex, white = hypothalamus.

connectivity are higher for diseased aging at month 4 ($p_{\text{Hypothalamic lateral zone-Striatum-like amygdalar nuclei}} = 0.021$, $p_{\text{Hypothalamic lateral zone-Fundus of striatum}} = 0.019$, $p_{\text{Midline group of the dorsal thalamus-Striatum-like amygdalar nuclei}} = 0.007$, $p_{\text{Anterior group of the dorsal thalamus-Striatum-like amygdalar nuclei}} = 8.64\ e\text{-}2$)(**Figure 2**).

All segregated datasets and the resultant statistics had a linear mixed effect model to estimate the coefficients of disease. Thus, the fixed effect is genotype, and the random effect are the subjects. Then a two-tailed t test is run to test the significance of the estimated coefficient. All statistics in this section was not corrected for multiple comparisons.

Thalamus and hypothalamus systems exhibit early-disease hyperconnectivity with other brain anatomical systems followed by suppression at later disease stages. We grouped ROIs and their relevant functional connectivity values into anatomical systems in order to evaluate the effect of disease progression on inter and intra system connectivity. One feature to note is that month 1.5 and month 2 exhibit different anatomical network profiles even though both timepoints are associated with the early stage of disease development (**Figure 3A**). There is cerebral accumulation of Amyloid plaques that at months 1.5 and 2 (42, 43). However, the difference in concentration between the two points is steep and so month 2 can be used as a proxy to

describe a later stage in disease development (43) relative to month 1.5. This feature is reflected in how markedly different the two anatomical networks are, where there is a clear difference in the number of depressed anatomical connectivity values for 5xFAD versus the control (**Figure 3A,B**). Once again, we note that the thalamic-hypothalamic region in month 2 exhibits a net positive connectivity value in the disease group even though the difference was not found to be significant ($p = 0.2570$ uncorrected). The systems at month 1.5, however, exhibit all intra-system functional connectivity, excluding the thalamic-thalamic connectivity, to be depressed for the 5xFAD class (**Figure 3A,B**). All inter and intra connectivity values were found to statistically insignificant ($p > 0.05$ when corrected for multiple comparisons), and only a handful were shown to be different between the disease and control group at both time points: striatum pallidum-hypothalamus ($p = 0.0131$ uncorrected, $p = 0.1726$ FDR corrected) for month 1.5, and intra striatum pallidum connectivity ($p= 0.0243$ uncorrected, $p = 0.1609$ FDR corrected) and Hippocampal-Heteromodal Cortex for month 2 ($p = 0.0494$ uncorrected, $p =0.1635$ FDR corrected). The lack of statistical significance when controlling for time falls in line with the projected timeline of disease pathology, where the early stages of disease development may not manifest significant changes to the anatomical networks. However, it must be stated that even though the differences between the two groups in each time point lacked significance, the average anatomical system network profiles were different, and strongly suggests that the increase in amyloid beta plaques could have had a role in influencing the net positive connectivity values for the disease group over the control group at month 2.

At month 4 we observe that the inter-system connectivity of the olfactory cortex and hippocampal region for the 5xFAD animal line is depressed relative to that of wildtype controls ($p = 0.0127$ uncorrected, $p = 0.3545$ FDR corrected) (**Figure 3 A,B**). What we also observed is that the depressed intra-hippocampal connectivity persists at month 6 ($p = 0.0011$ uncorrected, $p = 0.0164$ FDR corrected), and that a greater number of systems showed depressed intra-system connectivity at the later stage of disease, such as the sensorimotor cortex ($p = 0.0735$ uncorrected, $p = 0.0978$ FDR corrected), Hetermodal Cortex ($p = 0.0656$ uncorrected, $p = 0.0961$ FDR corrected), and Thalamus ($p = 0.01$ uncorrected, $p = 0.0487$ FDR corrected) (figure 3 A) There were a number of inter-system connectivity patterns that was implicated at the latest stage of disease, such as the Hypothalamus-Sensorimotor Cortex ($p = 0.0287$ uncorrected, $p = 0.06$ FDR corrected), Thalamus-Sensorimotor Cortex ($p = 0.0209$ uncorrected, $p = 0.059$ FDR corrected), Hypothalamus-Striatum Pallidum system ($p = 0.0474$ uncorrected, $p =0.0771$ FDR corrected, and Thalamus-Hippocampal connectivity ($p = 0.0040$ uncorrected, $p = 0.0292$ FDR corrected).

Statistics were conducted using a linear mixed effect model on timepoint segregated datasets. Thus, the fixed effect for each model is the genotype, and the random effect are the subjects. Thus, the estimated coefficients that describe the effect of disease on the response is statistically interrogated by a two-tailed t test.

Global brain networks become weaker, less integrated, and less efficient with disease progression. Given that prior analysis demonstrated that the ROIs implicated over disease progression did not remain consistent throughout the timepoints, and that the system level analysis yielded a similar perspective, we wanted to investigate how these different network profiles at different timepoints affected network integration and segregation. We utilized the Brain Connectivity Toolbox (50) to quantify metrics related to network integration and segregation where metrics such as global network clustering and assortativity indicating the degree of segregation, and shortest path and efficiency demonstrate integration. We first investigated how disease

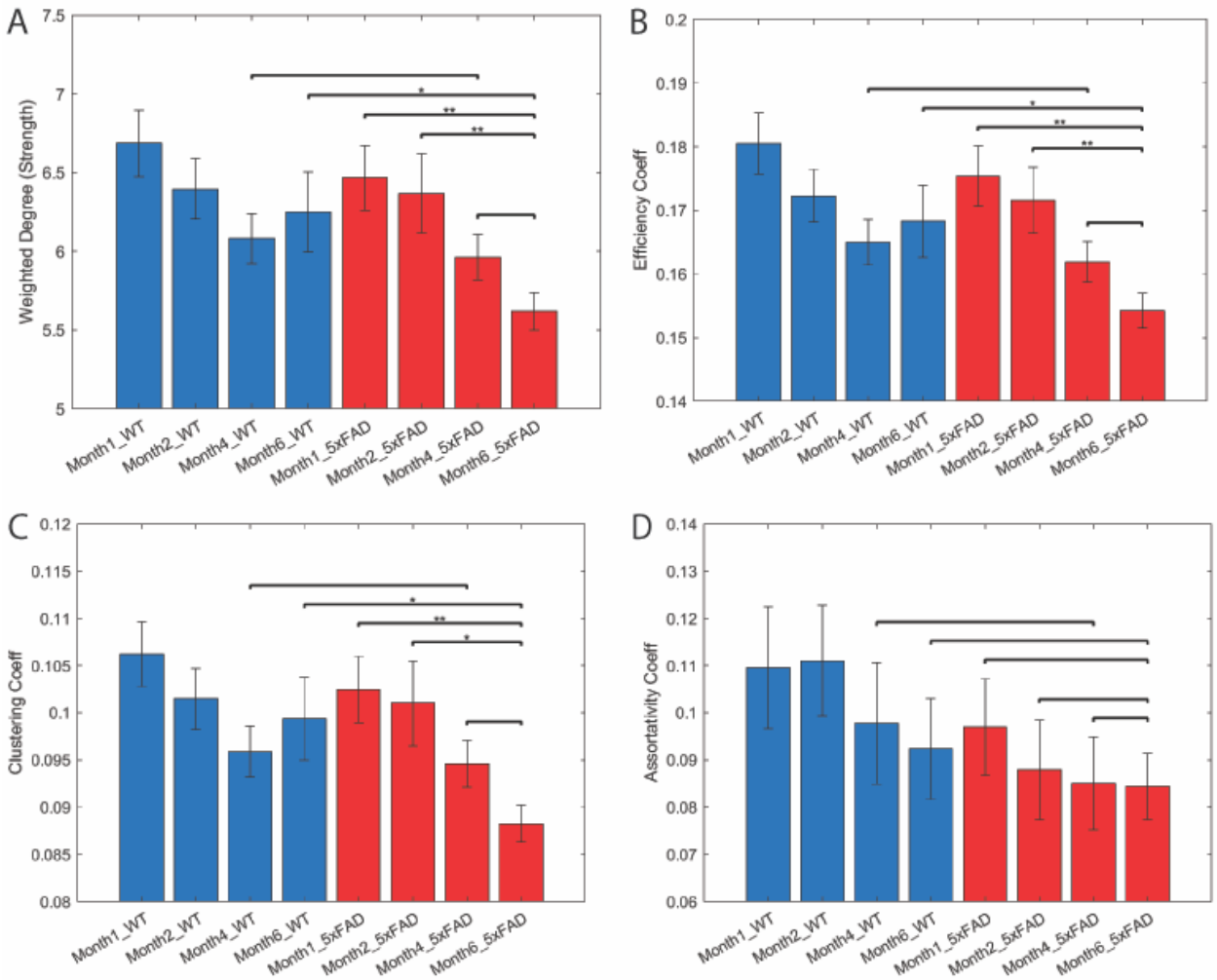

Figure 4. Global brain network is broadly negatively impacted by AD progression. Strength (A), efficiency (B), clustering coefficient (C), and assortativity (D) of the global brain network in transgenic AD (red) and wild-type littermate (blue) mice at the indicated ages. Error bars represent the standard error of the mean. Comparisons by two-tailed t test, *p< 0.05, **p< 0.005.

progression would affect network segregation and integration by first treating timepoints as a continuous variable and running a two-way ANCOVA. None of the interaction terms between genotype and timepoints were found to be statistically significant ($p_{strength}$ = 0.19458, $p_{charPath}$ = 0.2023, $p_{clustering}$ = 0.19342, $p_{efficiency}$ = 0.19037, $p_{assortativity}$ = 0.64371). However, given what we had observed in prior analysis regarding how the functional connectivity values did not follow a linear pattern over time, we then proceeded to investigate the degree to which disease state was correlated to changes in global network properties by treating each timepoint as a categorical class. The following analysis was conducted using a two-way ANOVA with genotype and timepoint as the factors.

Global network strength is shown to have differences at particular aging timepoints. The fully symptomatic state (timepoint month 6) exhibited a significantly lower degree of network strength than the early stages of disease development ($p_{5xFAD:M6 – 5xFAD: M1.5}$ = 0.005 and $p_{5xFAD:M6 – 5xFAD:M2}$ = 0.012), and that the disease development had a distinct effect on network strength when compared to healthy aging at the terminal time point ($p_{5xFAD:M6 – WT:M6}$ = 0.037) (**Figure 4A**). On the other hand, we did not observe any significant differences in network strength in healthy aging, and we note that network strength was not found to be different at the later stages of disease

development ($p_{5xFAD:M6 - 5xFAD:M4}$ = 0.252). Another metric that evaluates network integration is global efficiency, which is quantified as the inverse of the global characteristic path length between all nodes in the network (59). We observe the same pattern regarding global efficiency as global network strength. Healthy aged animals exhibited a different global level of efficiency than fully developed symptomatic mice ($p_{5xFAD:M6-WT:M6}$ = 0.036) (**Figure 4B**). What was surprising was that when controlling for age, we do not notice any differences in the networks efficiency until we compare fully aged animals against fully symptomatic animals, as such the intermediate state of disease development at month 4 exhibited insignificant differences at the efficiency metric relative to a healthy animal of the same age ($p_{5xFAD:M4-WT:M4}$ = 0.630).

Network integration metrics illustrate how well connected the nodes of the network are, and as a result one can infer how efficient information can be transferred across nodes, and what the ease of communication is between nodes (59, 67, 69). On the other hand, functional segregation allows one to infer how specialized certain regions of a network are. Such metrics can quantify groups and communities, some of which may exhibit special properties or functions depending on the context (59, 67, 68, 69). Therefore, we've quantified a metric of network segregation: clustering coefficient. Just like the global metrics of network integration, we observe similar trends regarding which age features differences between diseased and healthy animals (**Figure 4C**). Fully symptomatic animals had a lower clustering coefficient than that of healthy aged animals ($p_{5xFAD:M6-WT:M6}$ = 0.033), and that the later stages of disease development resulted in a lower clustering coefficient compared to early states of disease progression ($p_{5xFAD:M6-5xFAD: M1.5}$ = 0.007, $p_{5xFAD:M6-5xFAD: M2}$ = 0.013). Once again, the differences between the two groups is not observed at month 4 ($p_{5xFAD:M6-WT:M4}$ = 0.799).

Another metric of interest is assortativty. Assortativity can be interpreted as a metric that defines how one node exhibiting a set of characteristics tend to connect with other nodes with the same features (59, 69). Surprisingly, we do not observe any statistical differences between any groups and their respective timepoints. One interesting feature to note though is that at the beginning stage of disease development, we note that there is an appreciable difference in the Assortativity coefficient at month 1.5 ($p_{5xFAD:M1.5-WT:M1.5}$ = 0.421) (**Figure 4D**).

Statistics were conducted by using a two-tailed t test to interrogate if any significant difference exists between two metrics of interest (i.e. month 6 control versus month 6 wildtype). All graph theory metrics were derived using the Brain Connectivity Toolbox (50), and the graph metrics were quantified on every scan for every subject, before a subject average is quantified. Then the subjects' averages are pooled together to quantify an arithmetic mean.

Distinct regional cytokine signatures predict disease progression. There are regional differences regarding which cytokines drive aging for both diseased and healthy groups. We identify key cytokines driving aging in both disease and healthy groups separately, and have mapped a consensus cytokine list between the two groups per brain region based on cytokines that had a VIP score greater than 1 for at least one of the two groups (disease versus healthy). From there, we examined how different the loadings are for these cytokines of interest.

For the parietal cortex, we identify key cytokines upregulated in our disease model (3 LVs, p = 1.939 e-5, RMSECV = 22.201, **Figure 5A,B**) such as MIP-1α, MIP-1β and CXCL-1 (also known as keratinocyte-derived cytokine; KC). Thus, there is an upregulation of cytokines canonically associated with having a pro-inflammatory role (71, 72, 73, 74, 75) for diseased aging in the Parietal Cortex. However, in the healthy aging group (1 LV, p = 9.399 e-5, RMSECV = 43.202, figure 5C), we note that there is an upregulation of cytokines canonically associated with immune

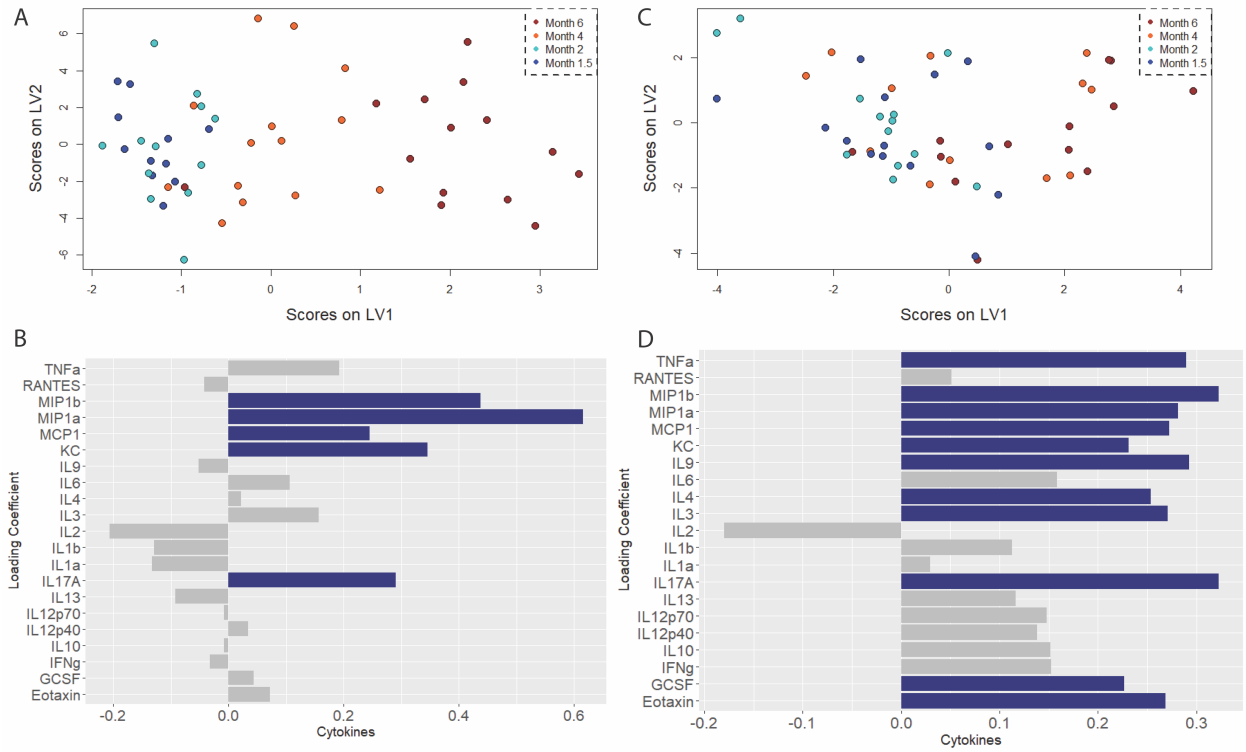

Figure 5. Parietal cortex exhibits progressive and specific up-regulation of microglial activation signature coinciding with onset of synaptic dysfunction. A) Scores plot and B) loadings on the first latent variable of an orthogonalized partial least squares regression model of cytokine levels in the parietal cortex regressed against age as a measurement of disease progression. C) Scores plot and D) loadings plot for the companion model in wild-type littermates. Colored bars indicate cytokines with VIP score > 1.

regulation such as MCP-1, GCSF, IL-4 and IL-9, and may exhibit neuroprotective roles (76, 77, 78, 79, 80, 84) in the brain. One key note is that these 'neuroprotective' cytokines are not seen as a covariate that drives aging in the disease group, but are in the healthy group. Another feature is that MIP-1α is significantly more upregulated in the disease group compared to the control group. It is observed that cytokines predominantly associated with inflamed environments such as TNF- α, Eotaxin, MIP-1α, and MIP-1β and IL-9 (74, 75, 81, 82, 83) are upregulated in healthy aging as well (**Figure 5C,D**). Therefore, there is some overlap between the two groups with regards to aging and the cytokine signatures that covary along with it. One surprising observation is that there are more VIP cytokines for healthy aging than there are for diseased aging, with 11 VIP cytokines for the control group, and only 5 for the diseased group.

Other brain regions such as the Frontal Cortex displayed a different cytokine signature, but similar pattern, that covaried with age. We note that IL-17A (or also known as IL-17), CXCL-1, and MIP-1β are upregulated in disease aging/disease progression (disease model had 2 LVs, p = 2.120 e-2, RMSECV = 30.391, **Figure 6A**). We also observe that IL-2, a cytokine that has shown to have a regulatory role in inflammation and neuronal activation (85-87), is downregulated in the diseased brain (**Figure 6B**). RANTES is also seen to be downregulated in diseased aging, and interestingly enough there is literature demonstrating that RANTES and IL-2 may have a synergistic relationship to promote an 'optimal' inflammatory response (88, 89), thus suggesting that the downregulation of the two in the diseased group, but elevation of RANTES and a no-factor effect of IL-2 in healthy aging suggests that the two may form a neuroprotective role within the context of the 5xFAD disease development timeline. In contrast to the diseased group, healthy aging of the Frontal Cortex involves significantly more cytokines (as determined by the VIP score,

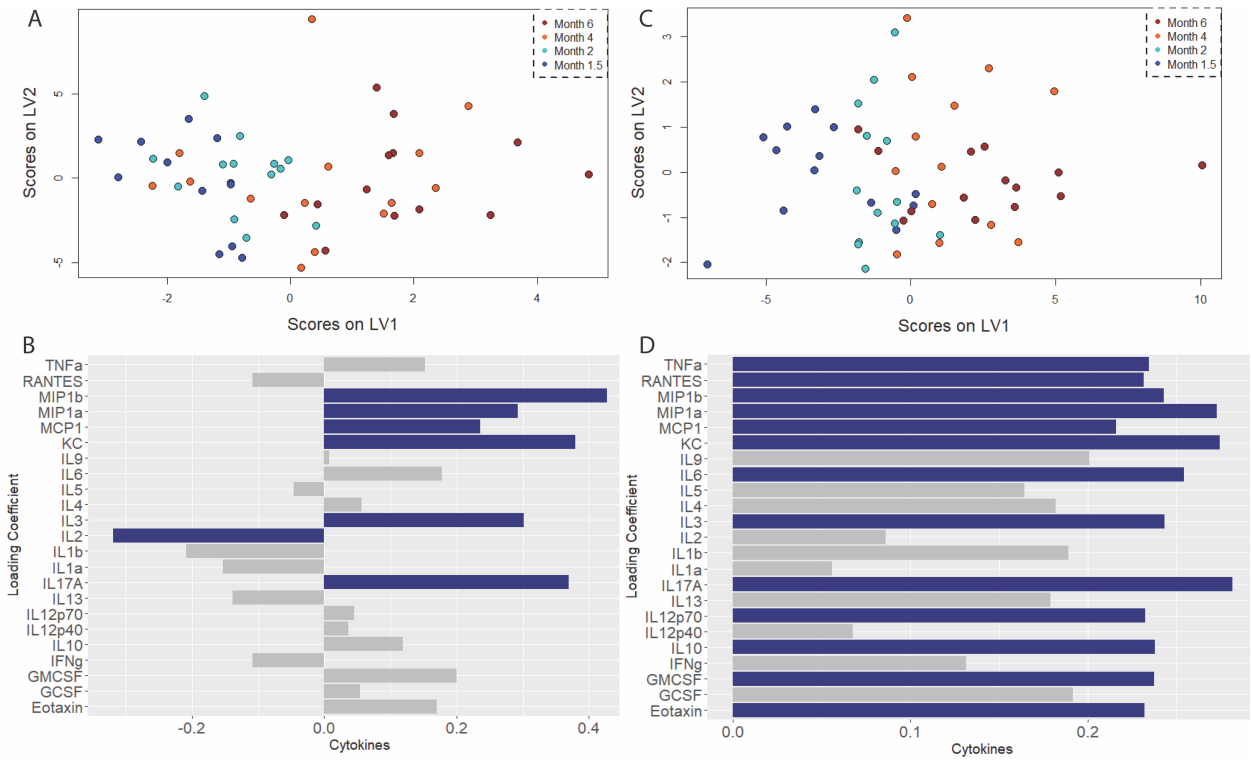

Figure 6. Temporal cortex exhibits progressive and specific up-regulation of microglial activation signature coinciding with onset of cognitive deficit. A) Scores plot and B) loadings on the first latent variable of an orthogonalized partial least squares regression model of cytokine levels in the temporal cortex regressed against age as a measurement of disease progression. C) Scores plot and D) loadings plot for the companion model in wild-type littermates. Colored bars indicate cytokines with VIP score > 1.

and their relative loading weight to the disease group) with 13 cytokines being labeled as covariates that drove the variance in healthy aging (1 LV, p = 3.474 e-5, RMSECV = 37.921, **Figure 6C**). The disease model only had 7 cytokines with the same interpretation. Thus, relative to the 5xFAD group, healthy aging has IL-10, Eotaxin, RANTES, IL12-p70 and IL-5 to be more upregulated. Interestingly enough, the profile here consists of cytokines canonically associated with inflammation such as Eotaxin and RANTES (82, 89, 90), and those that are seen as regulators of the inflammatory environment such as IL-10 and IL12-p70 (91, 92, 93). Interestingly enough, just like the observation made for healthy aging in the Parietal Cortex, the Frontal Cortex seems to have more cytokines that covary with age relative to disease progression (**Figure 6D**).

The temporal cortex also exhibits a similar pattern, but different cytokine signature, to the Frontal and Parietal Cortex. The disease model (1 LV, p =2.995 e-3, RMSECV = 30.238, **Figure 7A**) is shown to have RANTES, MIP-1α, MIP-1β, and IL-17A to be upregulated, While having IL12p70 to be down regulated (**Figure 7B**). By comparison, the healthy aging model (2 LVs, p = 7.074 e-6, RMSECV = 35.251, **Figure 7C**) has a myriad of cytokines that are upregulated and covary in the same direction as aging. Notable ones would be CCL1 (KC), IL5, IL6, IL12p70, IL17A, and interestingly enough TNF-α (**Figure 7D**). Thus, the temporal cortex cytokine profile for healthy aging is a mixture of both inflammatory and anti-inflammatory proteins (73, 82, 89, 90-94), a mixture that is distinct when comparing it to the other two cortical regions. The VIP cytokines in the disease model have common features to the cytokines profiles of the Frontal and Parietal cortex, with the commonality being MIP-1α, MIP-1β, and IL17A all being upregulated, and are classified as important covariates, with relation to disease development. Just like the healthy aging models for the Parietal and Frontal Cortex, the Temporal Cortex healthy aging model has

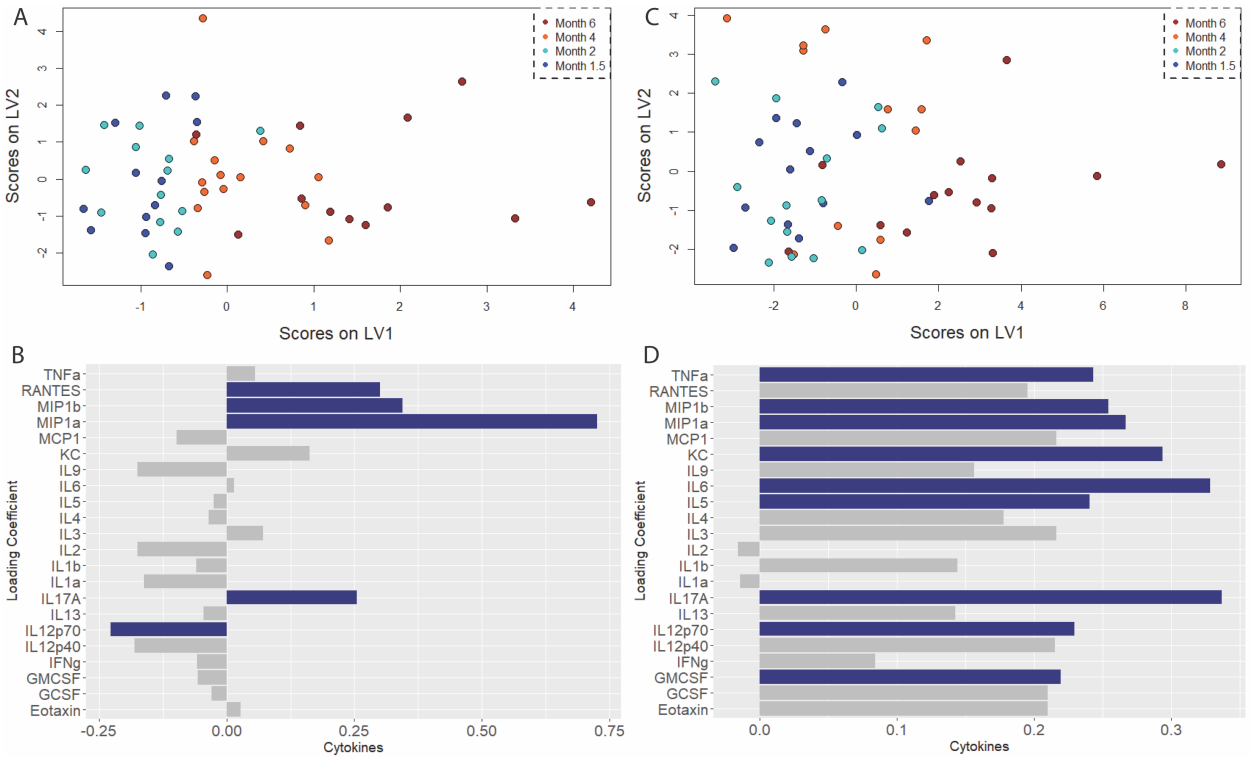

Figure 7. Frontal cortex exhibits progressive and specific up-regulation of microglial activation signature coinciding with onset of cognitive deficit. A) Scores plot and B) loadings on the first latent variable of an orthogonalized partial least squares regression model of cytokine levels in the frontal cortex regressed against age as a measurement of disease progression. C) Scores plot and D) loadings plot for the companion model in wild-type littermates. Colored bars indicate cytokines with VIP score > 1.

significantly more cytokines that have their expression in the brain region positively covary with age, with 9 cytokines being VIP in the healthy aging model, and only 5 in the disease model.

Discussion

The understanding of Alzheimer's Disease and its etiology is still incomplete, and the consequence of this is the impedance of therapeutic strategies that could successfully reverse AD pathology (70). As such we have sought to expand the existing understanding on how the progression of the neurodegenerative disease afflicts cognitive networks as the ultimate objective would be to ameliorate the impairments that occur over the development of Alzheimer's Disease. The reason for this is because Alzheimer's proteinpathy does not necessitate mortality, and instead it leads to other conditions that increase the risk of mortality such as the inability to take care of one's self, increased risky behavior (97), and the inability of basic physical functions such as the ability to swallow ingested food, leading to pneumonia (95, 96). Therefore, we have executed a comprehensive, multi-modal experiment to quantify two features of Alzheimer's Disease; the changes in cognitive networks over disease progression, and chronic neuroinflammation in the presence of AD pathology (64, 102-105).

There is extensive literature demonstrating how functional networks are altered between fully symptomatic AD patients and their respective healthy controls (98-101). However, one key feature that is missing is how functional networks are modulated over the progression of AD, excluding information on how and when the global network may be losing the ability to have segregated,

and specialized networks that could contribute to executing complex cognitive tasks (106-108). To fill this gap in our understanding of AD development, we have used a well stereotyped mouse model of AD and quantified its respective network metrics at 4 distinct time points (Figure 2) that correlate to disease states (42-46, 109). Our findings show that early disease pathology at months 1.5 and 2 exhibit profound changes to networks involving the thalamus and striatum/pallidum. Both the anatomical system and the individual ROIs within the Striatum/Pallidum, and Thalamus exhibited significant differences between the disease and healthy aging group. This is of particular interest given the roles of these two brain regions regarding cognitive functions. Firstly, the striatum and pallidum are part of the basal ganglia, a region that has the primary role of regulating motor control, and a role in higher order cognitive functions such as emotional processing and reward behavior (111-113). The thalamus, on the other hand is highly integrated within the central nervous system. Thus, it is commonly interpreted that the Thalamus plays a major role in multiple cognitive functions. For example, the Thalamus receives neuromodulatory inputs and excitatory inputs from a myriad of brain regions, including the basal ganglia (114-119, 122), and the lesion of the Thalamus has resulted in cognitive impairments such as executive dysfunction (120), and attention deficits (121). Research into other forms of cognitive impairments such as the classical Mild Cognitive Impairment stage (MCI) reinforce the importance of the Basal Ganglia and the Thalamus in cognitive health. It has been demonstrated that Basal Ganglia dysfunction is correlated with lower metrics of cognitive health (120, 121, 123-125). Thalamic hyper connectivity with cortical regions is associated with cognitive defects in schizophrenic subjects (126, 127). Therefore, given the highly integrated nature of the Thalamus and Basal Ganglia in cognitive functions, it is of particular interest to note that our results indicate changes to Thalamic and Basal Ganglia ROIs functional connectivity at the earliest stage of disease development. This would suggest that these brain regions are afflicted early at the disease stage. One potential reason for this would be that both regions feature efferent connections from the cortex (114, 122, 126). This feature is important since intraneuronal amyloid beta accumulates in the cortex of 5xFAD mice at months 1.5 (43), leading to a potential spillover to brain regions that have bijective connections to the afflicted cortical regions; like the Thalamus and Basal Ganglia.

Another finding of our experiment is that intra-hippocampal connectivity is depressed relative to healthy aging. Both individual ROIs and at the anatomical system level exhibit the depressed connectivity characteristic. This is in line with current literature as the hippocampus is the predominant brain region known to be afflicted in Alzheimer's Disease (43, 64, 129-132). What our results do provide new insight into is how inter hippocampal connectivity to the thalamus and striatum are impacted in the prodromal stage of disease development. Therefore, our findings are in line with existing literature detailing how there are return projections from the thalamus to the hippocampus (147), and that the two may have a synergistic role in the formation of memories (148). Additionally, it has been shown that the dorsal lateral striatum and the hippocampus may both have roles in information storage (149, 150).

Furthermore, our results provide insight as to how the global network architecture is modulated at different disease stages. We observe that the fully symptomatic disease state exhibits a lower degree of network integration and segregation relative to the healthy aging group. As the ability to segregate into specialized nodes corresponds to the ability to execute cognitive tasks (106-108), it is of extreme interest to observe how both aging and disease aging both have decreased levels of network segregation, and that the disease effect is more profound in decreasing the network's level of segregation and integration. Similar results have been observed in human studies as well, where heightened disease pathology is associated with lower levels of functional

segregation (60, 101, 133). The same trend for network integration was also observed in our results, with network efficiency decreasing in both disease and healthy aging, and that the fully symptomatic timepoint resulted in a significant difference in network efficiency. Studies that have explored network integration over the course of aging have found that expanded cognitive ability coincides with higher levels of network integration, and that aging itself is correlated with decreased cognitive functionality and levels of integration and segregation (134, 135). The interesting observation from our findings is that it is only at the terminal timepoint do these differences in network metrics exist between healthy and diseased aging. None of the metrics we've quantified demonstrate an appreciable difference at month 4, also known as the mid-late stage disease development. However, it is between the late stage to fully developed pathological state do the differences between healthy aging and AD progression arise. The fact that the differences in network characteristics manifest so late in disease development isn't a total surprise given that age is one of the major risk factors for developing sporadic AD. Our results reflect similarities in these global metrics in aging, but the difference at the terminal time point could be explained by how healthy aging brains may be able to compensate for age-related functionality declines (136, 137). It is extremely likely that the diseased brain is unable to undertake such processes given the breadth of tissue damage as a result of chronic inflammation due to disease pathology (43, 64, 86, 129-132, 138).

Lastly, our findings show distinct cytokine profiles for different brain regions: Temporal Cortex, Parietal Cortex, and the Frontal Cortex. Some of cytokines expressed in their unique signatures for diseased aging are commonly found in AD contexts such as MIP-1α, and MIP-1β (139, 140). However other key cytokines typically associated with AD such as IFN-γ, TNF-α, IL-1 (141) were not found in our measured signatures. That is not to say that the listed cytokines did not exist, but that these cytokines did not covary significantly with respect to time. While the different disease models share common cytokines, they also feature cytokines unique to their own respective models. MCP-1 is upregulated in the Parietal Cortex only, While IL-2 is downregulated in the Frontal Cortex, and IL12-p70 is downregulated for the Temporal Cortex. These small differences demonstrate the different aspects between the regional disease models. MCP-1 is a chemokine expressed by microglia (143), and knocking out MCP-1 from transgenic mice has been correlated to making the animals resistant to neurodegeneration (144). However, the downregulation of IL-2 and IL12-p70 in the other two cortices suggest that disease progression may progress differently in those brain regions relative to the Parietal Cortex. The reason for this hypothetical is because IL-2 and IL12-p70 are canonically associated with neuroprotective roles (88, 89, 92, 93). The regional cytokine profiles of disease progression give credence to the empirical evidence that different cortical lobes experience brain atrophy at different rates over the progression of AD. It has been shown that the parietal lobe experiences greater levels of atrophy at the prodromal stages of AD, While the frontal cortex is shown to experience damage at later stages with a lower degree of atrophy (145, 146). The regional specific rate of atrophy, and the regional specific cytokine signatures from our results indicate that the varying degree of disease pathology and its corresponding consequences are mediated by the expression of neuroprotective cytokines. It is only at the later stages of disease development do the expression of IL-2 and IL12-p70 fall off, which lines up with existing literature on how the frontal lobe atrophies at a slower, and at a later timepoint relative to the Parietal cortex. Our results also elucidated healthy aging and the corresponding cytokine signature. A qualitative commonality between the brain regions is that the healthy aging cytokine profile is more comprehensive than their diseased counterparts; featuring almost twice the number of cytokines than those featured in diseased model. Even though the heathy aging models featured canonically proinflammatory cytokines such as TNF-α, MIP-1α,

MIP-1β, and CCXL1 (71-75, 83), the healthy signatures also featured at least one anti-inflammatory cytokine such IL12-p70 (92, 93) for the Frontal and Temporal cortex, and IL-4 (76, 78) for the Parietal Cortex. It is possible that the upregulation of both anti and pro inflammatory cytokines may produce the desired neuroprotective effect, as shown in the synergistic relationship between IL-2 and RANTES (88, 89). We observe a similar trend regarding IL-2 and RANTES in the frontal cortex for diseased aging, where both RANTES and IL-2 are downregulated as a result of disease progression.

Conclusion

Here, we identify regional cortical specific cytokine signatures that are predictive of disease development. We also identify regions of interest where functional circuits could be potentially implicated in the early stages of Alzheimer's Disease. We also observe how network segregation and integration are impacted over disease development, and is in line with increasing disease pathology, in the form of neuroinflammation, in the cortical regions. All in all, we have elucidated how AD pathology can progressively impact the brain's network architecture, and the progressive changes to the architecture are correlated with increasing levels of neuroinflammation at the cortical regions of the brain.

Acknowledgements

This work was supported by R21AG068532 from the National Institute on Aging (EAP/NZ), grant TSF41000095613 from the Pennsylvania Department of Health using Tobacco CURE Funds (EAP/NZ), and start-up funds from Penn State College of Medicine Departments of Neurosurgery and Pharmacology (EAP). DCC and MKK were supported by training fellowship T32NS115667 from the National Neurological Disorders and Stroke. All funding agencies disclaim responsibility for any analyses, interpretations, or conclusions.

The co-authors would like to acknowledge the Huck Institutes' High Field Magnetic Resonance Imaging Core Facility (RRID:SCR_024461) and facility director Thomas Neuberger for helpful discussions in design of the imaging protocol.

The authors acknowledge help and advice from Samuel Cramer in restrainer design and testing; Said Hayreddin in building the surface imaging coil; Nikki Beloate in design of imaging post-processing procedure; and Kevin Turner in training for the headpost animal surgery.

References

1) 2023 Alzheimer's disease facts and figures. Alzheimers Dement. 2023;19(4):1598-1695. doi:10.1002/alz.13016

2) Hebert LE, Weuve J, Scherr PA, Evans DA. Alzheimer disease in the United States (2010-2050) estimated using the 2010 census. Neurology. 2013;80(19):1778-1783. doi:10.1212/WNL.0b013e31828726f5

3) Brookmeyer R, Johnson E, Ziegler-Graham K, Arrighi HM. Forecasting the global burden of Alzheimer's disease. Alzheimers Dement. 2007;3(3):186-191. doi:10.1016/j.jalz.2007.04.381

4) Stites SD, Harkins K, Rubright JD, Karlawish J. Relationships Between Cognitive Complaints and Quality of Life in Older Adults With Mild Cognitive Impairment, Mild Alzheimer Disease Dementia, and Normal Cognition. Alzheimer Dis Assoc Disord. 2018;32(4):276-283. doi:10.1097/WAD.0000000000000262

5) Pan, CW., Wang, X., Ma, Q. et al. Cognitive dysfunction and health-related quality of life among older Chinese. Sci Rep 5, 17301 (2015). https://doi.org/10.1038/srep17301

6) Hampel, H., Hardy, J., Blennow, K. et al. The Amyloid-β Pathway in Alzheimer's Disease. Mol Psychiatry 26, 5481–5503 (2021). https://doi.org/10.1038/s41380-021-01249-0

7) Li X, Ospitalieri S, Robberechts T, et al. Seeding, maturation and propagation of amyloid β-peptide aggregates in Alzheimer's disease. Brain. 2022;145(10):3558-3570. doi:10.1093/brain/awac202

8) Walsh DM, Klyubin I, Fadeeva JV, et al. Naturally secreted oligomers of amyloid beta protein potently inhibit hippocampal long-term potentiation in vivo. Nature. 2002;416(6880):535-539. doi:10.1038/416535a

9) Hsia AY, Masliah E, McConlogue L, et al. Plaque-independent disruption of neural circuits in Alzheimer's disease mouse models. Proc Natl Acad Sci U S A. 1999;96(6):3228-3233. doi:10.1073/pnas.96.6.3228

10) Spires-Jones TL, Meyer-Luehmann M, Osetek JD, et al. Impaired spine stability underlies plaque-related spine loss in an Alzheimer's disease mouse model. Am J Pathol. 2007;171(4):1304-1311. doi:10.2353/ajpath.2007.070055

11) Hsia AY, Masliah E, McConlogue L, et al. Plaque-independent disruption of neural circuits in Alzheimer's disease mouse models. Proc Natl Acad Sci U S A. 1999;96(6):3228-3233. doi:10.1073/pnas.96.6.3228

12) Walsh, D., Klyubin, I., Fadeeva, J. et al. Naturally secreted oligomers of amyloid β protein potently inhibit hippocampal long-term potentiation in vivo. Nature 416, 535–539 (2002). https://doi.org/10.1038/416535a

13) DeTure MA, Dickson DW. The neuropathological diagnosis of Alzheimer's disease. Mol Neurodegener. 2019;14(1):32. Published 2019 Aug 2. doi:10.1186/s13024-019-0333-5

14) Dickson DW. Neuropathological diagnosis of Alzheimer's disease: a perspective from longitudinal clinicopathological studies. Neurobiol Aging. 1997;18(4 Suppl):S21-S26. doi:10.1016/s0197-4580(97)00065-1

15) Akiyama H, Barger S, Barnum S, et al. Inflammation and Alzheimer's disease. Neurobiol Aging. 2000;21(3):383-421. doi:10.1016/s0197-4580(00)00124-x

16) Knopman, D.S., Amieva, H., Petersen, R.C. et al. Alzheimer disease. Nat Rev Dis Primers 7, 33 (2021). https://doi.org/10.1038/s41572-021-00269-y

17) DeTure MA, Dickson DW. The neuropathological diagnosis of Alzheimer's disease. Mol Neurodegener. 2019;14(1):32. Published 2019 Aug 2. doi:10.1186/s13024-019-0333-5

18) Dhawan G, Floden AM, Combs CK. Amyloid-β oligomers stimulate microglia through a tyrosine kinase dependent mechanism. Neurobiol Aging. 2012;33(10):2247-2261. doi:10.1016/j.neurobiolaging.2011.10.027

19) Nordengen, K., Kirsebom, BE., Henjum, K. et al. Glial activation and inflammation along the Alzheimer's disease continuum. J Neuroinflammation 16, 46 (2019). https://doi.org/10.1186/s12974-019-1399-2Frautschy SA, Yang F, Irrizarry M, et al. Microglial response to amyloid plaques in APPsw transgenic mice. Am J Pathol. 1998;152(1):307-317.

20) Kelley BJ, Petersen RC. Alzheimer's disease and mild cognitive impairment. Neurol Clin. 2007;25(3):577-v. doi:10.1016/j.ncl.2007.03.008

21) Kim CK, Lee YR, Ong L, Gold M, Kalali A, Sarkar J. Alzheimer's Disease: Key Insights from Two Decades of Clinical Trial Failures. J Alzheimers Dis. 2022;87(1):83-100. doi:10.3233/JAD-215699

22) Yiannopoulou KG, Anastasiou AI, Zachariou V, Pelidou SH. Reasons for Failed Trials of Disease-Modifying Treatments for Alzheimer Disease and Their Contribution in Recent Research. Biomedicines. 2019;7(4):97. Published 2019 Dec 9. doi:10.3390/biomedicines7040097

23) Venugopalan J, Tong L, Hassanzadeh HR, Wang MD. Multimodal deep learning models for early detection of Alzheimer's disease stage. Sci Rep. 2021;11(1):3254. Published 2021 Feb 5. doi:10.1038/s41598-020-74399-w

24) Ezzati A, Lipton RB; Alzheimer's Disease Neuroimaging Initiative. Machine Learning Predictive Models Can Improve Efficacy of Clinical Trials for Alzheimer's Disease. J Alzheimers Dis. 2020;74(1):55-63. doi:10.3233/JAD-190822

25) Diogo, V.S., Ferreira, H.A., Prata, D. et al. Early diagnosis of Alzheimer's disease using machine learning: a multi-diagnostic, generalizable approach. Alz Res Therapy 14, 107 (2022). https://doi.org/10.1186/s13195-022-01047-y

26) Venugopalan, J., Tong, L., Hassanzadeh, H.R. et al. Multimodal deep learning models for early detection of Alzheimer's disease stage. Sci Rep 11, 3254 (2021). https://doi.org/10.1038/s41598-020-74399-w

27) Ren S, Yao W, Tambini MD, Yin T, Norris KA, D'Adamio L. Microglia TREM2R47H Alzheimer-linked variant enhances excitatory transmission and reduces LTP via increased TNF-α levels. Elife. 2020;9:e57513. Published 2020 Jun 24. doi:10.7554/eLife.57513

28) Nguyen PT, Dorman LC, Pan S, et al. Microglial Remodeling of the Extracellular Matrix Promotes Synapse Plasticity. Cell. 2020;182(2):388-403.e15. doi:10.1016/j.cell.2020.05.050

29) Liu T, Jiang CY, Fujita T, Luo SW, Kumamoto E. Enhancement by interleukin-1β of AMPA and NMDA receptor-mediated currents in adult rat spinal superficial dorsal horn neurons. Mol Pain. 2013;9:16. Published 2013 Mar 28. doi:10.1186/1744-8069-9-16

30) Jung, H., Lee, D., You, H. et al. LPS induces microglial activation and GABAergic synaptic deficits in the hippocampus accompanied by prolonged cognitive impairment. Sci Rep 13, 6547 (2023). https://doi.org/10.1038/s41598-023-32798-9

31) Biswal B, Yetkin FZ, Haughton VM, Hyde JS. Functional connectivity in the motor cortex of resting human brain using echo-planar MRI. Magn Reson Med. 1995;34(4):537-541. doi:10.1002/mrm.1910340409

32) Hayes SM, Ryan L, Schnyer DM, Nadel L. An fMRI study of episodic memory: retrieval of object, spatial, and temporal information. Behav Neurosci. 2004;118(5):885-896. doi:10.1037/0735-7044.118.5.885

33) Pessoa L, Gutierrez E, Bandettini P, Ungerleider L. Neural correlates of visual working memory: fMRI amplitude predicts task performance. Neuron. 2002;35(5):975-987. doi:10.1016/s0896-6273(02)00817-6

34) Busche MA, Konnerth A. Impairments of neural circuit function in Alzheimer's disease. Philos Trans R Soc Lond B Biol Sci. 2016;371(1700):20150429. doi:10.1098/rstb.2015.0429

35) Filippini N, MacIntosh BJ, Hough MG, et al. Distinct patterns of brain activity in young carriers of the APOE-epsilon4 allele. Proc Natl Acad Sci U S A. 2009;106(17):7209-7214. doi:10.1073/pnas.0811879106

36) Greicius MD, Krasnow B, Reiss AL, Menon V. Functional connectivity in the resting brain: a network analysis of the default mode hypothesis. Proc Natl Acad Sci U S A. 2003;100(1):253-258. doi:10.1073/pnas.0135058100

37) Raichle ME, MacLeod AM, Snyder AZ, Powers WJ, Gusnard DA, Shulman GL. A default mode of brain function. Proc Natl Acad Sci U S A. 2001;98(2):676-682. doi:10.1073/pnas.98.2.676

38) Franzmeier N, Caballero MÁA, Taylor ANW, et al. Resting-state global functional connectivity as a biomarker of cognitive reserve in mild cognitive impairment. Brain Imaging Behav. 2017;11(2):368-382. doi:10.1007/s11682-016-9599-1

39) Dai C, Zhang Y, Cai X, et al. Effects of Sleep Deprivation on Working Memory: Change in Functional Connectivity Between the Dorsal Attention, Default Mode, and Fronto-Parietal Networks. Front Hum Neurosci. 2020;14:360. Published 2020 Oct 12. doi:10.3389/fnhum.2020.00360

40) Pievani, M., Filippini, N., van den Heuvel, M. et al. Brain connectivity in neurodegenerative diseases—from phenotype to proteinopathy. Nat Rev Neurol 10, 620–633 (2014). https://doi.org/10.1038/nrneurol.2014.178

41) 5xFAD (B6SJL) | ALZFORUM. www.alzforum.org. https://www.alzforum.org/research-models/5xfad-b6sjl

42) Oakley H, Cole SL, Logan S, et al. Intraneuronal beta-amyloid aggregates, neurodegeneration, and neuron loss in transgenic mice with five familial Alzheimer's disease mutations: potential factors in amyloid plaque formation. J Neurosci. 2006;26(40):10129-10140. doi:10.1523/JNEUROSCI.1202-06.2006

43) Bader AS, Gnädig MU, Fricke M, et al. Brain Region-Specific Differences in Amyloid-β Plaque Composition in 5XFAD Mice. Life (Basel). 2023;13(4):1053. Published 2023 Apr 20. doi:10.3390/life13041053

44) Eimer, W.A., Vassar, R. Neuron loss in the 5XFAD mouse model of Alzheimer's disease correlates with intraneuronal Aβ42 accumulation and Caspase-3 activation. Mol Neurodegeneration 8, 2 (2013). https://doi.org/10.1186/1750-1326-8-2

45) Poon CH, Wong STN, Roy J, et al. Sex Differences between Neuronal Loss and the Early Onset of Amyloid Deposits and Behavioral Consequences in 5xFAD Transgenic Mouse as a Model for Alzheimer's Disease. Cells. 2023;12(5):780. Published 2023 Mar 1. doi:10.3390/cells12050780

46) Liu Y, Perez PD, Ma Z, et al. An open database of resting-state fMRI in awake rats. Neuroimage. 2020;220:117094. doi:10.1016/j.neuroimage.2020.117094

47) Dopfel, D., Perez, P.D., Verbitsky, A. et al. Individual variability in behavior and functional networks predicts vulnerability using an animal model of PTSD. Nat Commun 10, 2372 (2019). https://doi.org/10.1038/s41467-019-09926-z

48) SPM - Statistical Parametric Mapping. Ucl.ac.uk. Published 2023. https://fil.ion.ucl.ac.uk/spm/

49) Rubinov M, Sporns O. Complex network measures of brain connectivity: uses and interpretations. Neuroimage. 2010;52(3):1059-1069. doi:10.1016/j.neuroimage.2009.10.003

50) van den Heuvel MP, Mandl RC, Stam CJ, Kahn RS, Hulshoff Pol HE. Aberrant frontal and temporal complex network structure in schizophrenia: a graph theoretical analysis. J Neurosci. 2010;30(47):15915-15926. doi:10.1523/JNEUROSCI.2874-10.2010

51) Sporns O. Graph theory methods: applications in brain networks. Dialogues Clin Neurosci. 2018;20(2):111-121. doi:10.31887/DCNS.2018.20.2/osporns

52) Onnela JP, Saramäki J, Kertész J, Kaski K. Intensity and coherence of motifs in weighted complex networks. Phys Rev E Stat Nonlin Soft Matter Phys. 2005;71(6 Pt 2):065103. doi:10.1103/PhysRevE.71.065103

53) Brandes U. A faster algorithm for betweenness centrality*. The Journal of Mathematical Sociology. 2001;25(2):163-177. doi:https://doi.org/10.1080/0022250x.2001.9990249

54) Watts, D., Strogatz, S. Collective dynamics of 'small-world' networks. Nature 393, 440–442 (1998). https://doi.org/10.1038/30918

55) Latora V, Marchiori M. Efficient behavior of small-world networks. Phys Rev Lett. 2001;87(19):198701. doi:10.1103/PhysRevLett.87.198701

56) Newman MEJ. Assortative Mixing in Networks. Physical Review Letters. 2002;89(20). doi:https://doi.org/10.1103/physrevlett.89.208701

57) Kuhn MK, Fleeman RM, Beidler LM, Snyder AM, Chan DC, Proctor EA. Amyloid-β Pathology-Specific Cytokine Secretion Suppresses Neuronal Mitochondrial Metabolism. Cell Mol Bioeng. 2023;16(4):405-421. Published 2023 Sep 11. doi:10.1007/s12195-023-00782-y

58) Fleeman RM, Snyder AM, Kuhn MK, et al. Predictive link between systemic metabolism and cytokine signatures in the brain of apolipoprotein E ε4 mice. Neurobiol Aging. 2023;123:154-169. doi:10.1016/j.neurobiolaging.2022.11.015

59) Steward A, Biel D, Brendel M, et al. Functional network segregation is associated with attenuated tau spreading in Alzheimer's disease. Alzheimers Dement. 2023;19(5):2034-2046. doi:10.1002/alz.12867

60) Ewers M, Luan Y, Frontzkowski L, et al. Segregation of functional networks is associated with cognitive resilience in Alzheimer's disease. Brain. 2021;144(7):2176-2185. doi:10.1093/brain/awab112

61) Wold S, Ruhe A, Wold H, Dunn, III WJ. The Collinearity Problem in Linear Regression. The Partial Least Squares (PLS) Approach to Generalized Inverses. SIAM Journal on Scientific and Statistical Computing. 1984;5(3):735-743. doi:https://doi.org/10.1137/0905052

62) Thevenot EA, Roux A, Xu Y, Ezan E, Junot C (2015). “Analysis of the human adult urinary metabolome variations with age, body mass index and gender by implementing a comprehensive workflow for univariate and OPLS statistical analyses.” Journal of Proteome Research, 14, 3322-3335. https://doi.org/10.1021/acs.jproteome.5b00354.

63) Kuhn MK, Fleeman RM, Beidler LM, Snyder AM, Chan DC, Proctor EA. Alzheimer's disease-specific cytokine secretion suppresses neuronal mitochondrial metabolism. Preprint. bioRxiv. 2023;2023.04.07.536014. Published 2023 Apr 7. doi:10.1101/2023.04.07.536014

64) Trygg J, Wold S. Orthogonal projections to latent structures (O-PLS). Journal of Chemometrics. 2002;16(3):119-128. doi:https://doi.org/10.1002/cem.695

65) Galindo-Prieto B, Eriksson L, Trygg J. Variable influence on projection (VIP) for orthogonal projections to latent structures (OPLS). Journal of Chemometrics. 2014;28(8):623-632. doi:https://doi.org/10.1002/cem.2627

66) Barrat A, Barthélemy M, Pastor-Satorras R, Vespignani A. The architecture of complex weighted networks. Proc Natl Acad Sci U S A. 2004;101(11):3747-3752. doi:10.1073/pnas.0400087101

67) Achard S, Bullmore E. Efficiency and cost of economical brain functional networks. PLoS Comput Biol. 2007;3(2):e17. doi:10.1371/journal.pcbi.0030017

68) Hanisch D, Zien A, Zimmer R, Lengauer T. Co-clustering of biological networks and gene expression data. Bioinformatics. 2002;18 Suppl 1:S145-S154. doi:10.1093/bioinformatics/18.suppl_1.s145

69) Kim CK, Lee YR, Ong L, Gold M, Kalali A, Sarkar J. Alzheimer's Disease: Key Insights from Two Decades of Clinical Trial Failures. J Alzheimers Dis. 2022;87(1):83-100. doi:10.3233/JAD-215699

70) Sui Y, Potula R, Dhillon N, et al. Neuronal apoptosis is mediated by CXCL10 overexpression in simian human immunodeficiency virus encephalitis. Am J Pathol. 2004;164(5):1557-1566. doi:10.1016/S0002-9440(10)63714-5

71) Sui Y, Stehno-Bittel L, Li S, et al. CXCL10-induced cell death in neurons: role of calcium dysregulation. Eur J Neurosci. 2006;23(4):957-964. doi:10.1111/j.1460-9568.2006.04631.x

72) Vlkolinský R, Siggins GR, Campbell IL, Krucker T. Acute exposure to CXC chemokine ligand 10, but not its chronic astroglial production, alters synaptic plasticity in mouse hippocampal slices. J Neuroimmunol. 2004;150(1-2):37-47. doi:10.1016/j.jneuroim.2004.01.011

73) Bhavsar I, Miller CS, Al-Sabbagh M. Macrophage Inflammatory Protein-1 Alpha (MIP-1 alpha)/CCL3: As a Biomarker. General Methods in Biomarker Research and their Applications. 2015;223-249. Published 2015 Jun 1. doi:10.1007/978-94-007-7696-8_27

74) Marciniak, E., Faivre, E., Dutar, P. et al. The Chemokine MIP-1α/CCL3 impairs mouse hippocampal synaptic transmission, plasticity and memory. Sci Rep 5, 15862 (2015). https://doi.org/10.1038/srep15862

75) Francos-Quijorna I, Amo-Aparicio J, Martinez-Muriana A, López-Vales R. IL-4 drives microglia and macrophages toward a phenotype conducive for tissue repair and functional recovery after spinal cord injury. Glia. 2016;64(12):2079-2092. doi:10.1002/glia.23041

76) Xue G, Jin G, Fang J, Lu Y. IL-4 together with IL-1β induces antitumor Th9 cell differentiation in the absence of TGF-β signaling. Nat Commun. 2019;10(1):1376. Published 2019 Mar 26. doi:10.1038/s41467-019-09401-9

77) Fenn AM, Hall JC, Gensel JC, Popovich PG, Godbout JP. IL-4 signaling drives a unique arginase+/IL-1β+ microglia phenotype and recruits macrophages to the inflammatory CNS: consequences of age-related deficits in IL-4Rα after traumatic spinal cord injury. J Neurosci. 2014;34(26):8904-8917. doi:10.1523/JNEUROSCI.1146-14.2014

78) Rahi V, Jamwal S, Kumar P. Neuroprotection through G-CSF: recent advances and future viewpoints. Pharmacol Rep. 2021;73(2):372-385. doi:10.1007/s43440-020-00201-3

79) Zambrano A, Otth C, Maccioni RB, Concha II. IL-3 controls tau modifications and protects cortical neurons from neurodegeneration. Curr Alzheimer Res. 2010;7(7):615-624. doi:10.2174/156720510793499011

80) Parajuli B, Horiuchi H, Mizuno T, Takeuchi H, Suzumura A. CCL11 enhances excitotoxic neuronal death by producing reactive oxygen species in microglia. Glia. 2015;63(12):2274-2284. doi:10.1002/glia.22892

81) Wakabayashi, K., Isozaki, T., Tsubokura, Y. et al. Eotaxin-1/CCL11 is involved in cell migration in rheumatoid arthritis. Sci Rep 11, 7937 (2021). https://doi.org/10.1038/s41598-021-87199-7

82) Donninelli G, Saraf-Sinik I, Mazziotti V, et al. Interleukin-9 regulates macrophage activation in the progressive multiple sclerosis brain. J Neuroinflammation. 2020;17(1):149. Published 2020 May 6. doi:10.1186/s12974-020-01770-z

83) Miñano FJ, Fernández-Alonso A, Myers RD, Sancibrián M. Hypothalamic interaction between macrophage inflammatory protein-1 alpha (MIP-1 alpha) and MIP-1 beta in rats: a new level for fever control?. J Physiol. 1996;491 (Pt 1)(Pt 1):209-217. doi:10.1113/jphysiol.1996.sp021208

84) Yshii, L., Pasciuto, E., Bielefeld, P. et al. Astrocyte-targeted gene delivery of interleukin 2 specifically increases brain-resident regulatory T cell numbers and protects against pathological

neuroinflammation. Nat Immunol 23, 878–891 (2022). https://doi.org/10.1038/s41590-022-01208-z

85) Alves S, Churlaud G, Audrain M, et al. Interleukin-2 improves amyloid pathology, synaptic failure and memory in Alzheimer's disease mice. Brain. 2017;140(3):826-842. doi:10.1093/brain/aww330

86) Meola D, Huang Z, Petitto JM. Selective Neuronal and Brain Regional Expession of IL-2 in IL2P 8-GFP Transgenic Mice: Relation to Sensorimotor Gating. J Alzheimers Dis Parkinsonism. 2013;3(4):1000127. doi:10.4172/2161-0460.1000127

87) Weiss JM, Back TC, Scarzello AJ, et al. Successful immunotherapy with IL-2/anti-CD40 induces the chemokine-mediated mitigation of an immunosuppressive tumor microenvironment. Proc Natl Acad Sci U S A. 2009;106(46):19455-19460. doi:10.1073/pnas.0909474106

88) Parisi, G., Saco, J.D., Salazar, F.B. et al. Persistence of adoptively transferred T cells with a kinetically engineered IL-2 receptor agonist. Nat Commun 11, 660 (2020). https://doi.org/10.1038/s41467-019-12901-3

89) Ivanovska M, Abdi Z, Murdjeva M, Macedo D, Maes A, Maes M. CCL-11 or Eotaxin-1: An Immune Marker for Ageing and Accelerated Ageing in Neuro-Psychiatric Disorders. Pharmaceuticals (Basel). 2020;13(9):230. Published 2020 Sep 2. doi:10.3390/ph13090230

90) Shanaki-Bavarsad M, Almolda B, González B, Castellano B. Astrocyte-targeted Overproduction of IL-10 Reduces Neurodegeneration after TBI. Exp Neurobiol. 2022;31(3):173-195. doi:10.5607/en21035

91) Andreadou, M., Ingelfinger, F., De Feo, D. et al. IL-12 sensing in neurons induces neuroprotective CNS tissue adaptation and attenuates neuroinflammation in mice. Nat Neurosci 26, 1701–1712 (2023). https://doi.org/10.1038/s41593-023-01435-z

92) Ishiguro, A., Suzuki, Y., Inaba, Y. et al. Production of Interleukin-10 in the Cerebrospinal Fluid in Aseptic Meningitis of Children. Pediatr Res 40, 610–614 (1996). https://doi.org/10.1203/00006450-199610000-00016

93) Frankola KA, Greig NH, Luo W, Tweedie D. Targeting TNF-α to elucidate and ameliorate neuroinflammation in neurodegenerative diseases. CNS Neurol Disord Drug Targets. 2011;10(3):391-403. doi:10.2174/187152711794653751

94) Kukull WA, Brenner DE, Speck CE, et al. Causes of death associated with Alzheimer disease: variation by level of cognitive impairment before death. J Am Geriatr Soc. 1994;42(7):723-726. doi:10.1111/j.1532-5415.1994.tb06531.x

95) Duan, J., Lv, YB., Gao, X. et al. Association of cognitive impairment and elderly mortality: differences between two cohorts ascertained 6-years apart in China. BMC Geriatr 20, 29 (2020). https://doi.org/10.1186/s12877-020-1424-4

96) Ha J, Kim EJ, Lim S, et al. Altered risk-aversion and risk-taking behaviour in patients with Alzheimer's disease. Psychogeriatrics. 2012;12(3):151-158. doi:10.1111/j.1479-8301.2011.00396.x

97) Stam CJ, de Haan W, Daffertshofer A, et al. Graph theoretical analysis of magnetoencephalographic functional connectivity in Alzheimer's disease. Brain. 2009;132(Pt 1):213-224. doi:10.1093/brain/awn262

98) Yao Z, Zhang Y, Lin L, et al. Abnormal cortical networks in mild cognitive impairment and Alzheimer's disease. PLoS Comput Biol. 2010;6(11):e1001006. Published 2010 Nov 18. doi:10.1371/journal.pcbi.1001006

99) Miraglia F, Vecchio F, Pappalettera C, et al. Brain Connectivity and Graph Theory Analysis in Alzheimer's and Parkinson's Disease: The Contribution of Electrophysiological Techniques. Brain Sci. 2022;12(3):402. Published 2022 Mar 18. doi:10.3390/brainsci12030402

100) Ng, A.S., Wang, J., Ng, K. et al. Distinct network topology in Alzheimer's disease and behavioral variant frontotemporal dementia. Alz Res Therapy 13, 13 (2021). https://doi.org/10.1186/s13195-020-00752-w

101) Bolmont T, Haiss F, Eicke D, et al. Dynamics of the microglial/amyloid interaction indicate a role in plaque maintenance. J Neurosci. 2008;28(16):4283-4292. doi:10.1523/JNEUROSCI.4814-07.2008

102) Baik SH, Kang S, Son SM, Mook-Jung I. Microglia contributes to plaque growth by cell death due to uptake of amyloid β in the brain of Alzheimer's disease mouse model. Glia. 2016;64(12):2274-2290. doi:10.1002/glia.23074

103) Simard AR, Soulet D, Gowing G, Julien JP, Rivest S. Bone marrow-derived microglia play a critical role in restricting senile plaque formation in Alzheimer's disease. Neuron. 2006;49(4):489-502. doi:10.1016/j.neuron.2006.01.022

104) Hickman SE, Allison EK, El Khoury J. Microglial dysfunction and defective beta-amyloid clearance pathways in aging Alzheimer's disease mice. J Neurosci. 2008;28(33):8354-8360. doi:10.1523/JNEUROSCI.0616-08.2008

105) Wang R, Liu M, Cheng X, Wu Y, Hildebrandt A, Zhou C. Segregation, integration, and balance of large-scale resting brain networks configure different cognitive abilities. Proc Natl Acad Sci U S A. 2021;118(23):e2022288118. doi:10.1073/pnas.2022288118

106) Machida K, Johnson KA. Integration and Segregation of the Brain Relate to Stability of Performance in Children and Adolescents with Varied Levels of Inattention and Impulsivity. Brain Connect. 2019;9(9):711-729. doi:10.1089/brain.2019.0671

107) Cohen JR, D'Esposito M. The Segregation and Integration of Distinct Brain Networks and Their Relationship to Cognition. J Neurosci. 2016;36(48):12083-12094. doi:10.1523/JNEUROSCI.2965-15.2016

108) Forner S, Kawauchi S, Balderrama-Gutierrez G, et al. Systematic phenotyping and characterization of the 5xFAD mouse model of Alzheimer's disease. Sci Data. 2021;8(1):270. Published 2021 Oct 15. doi:10.1038/s41597-021-01054-y

109) Zhang J, Wu N, Wang S, et al. Neuronal loss and microgliosis are restricted to the core of Aβ deposits in mouse models of Alzheimer's disease. Aging Cell. 2021;20(6):e13380. doi:10.1111/acel.13380

110) Haber SN, Kim KS, Mailly P, Calzavara R. Reward-related cortical inputs define a large striatal region in primates that interface with associative cortical connections, providing a substrate for incentive-based learning. J Neurosci. 2006;26(32):8368-8376. doi:10.1523/JNEUROSCI.0271-06.2006

111) Ceravolo, L., Frühholz, S., Pierce, J. et al. Basal ganglia and cerebellum contributions to vocal emotion processing as revealed by high-resolution fMRI. Sci Rep 11, 10645 (2021). https://doi.org/10.1038/s41598-021-90222-6

112) Hormigo S, Vega-Flores G, Castro-Alamancos MA. Basal Ganglia Output Controls Active Avoidance Behavior. J Neurosci. 2016;36(40):10274-10284. doi:10.1523/JNEUROSCI.1842-16.2016

113) Shine, J.M., Lewis, L.D., Garrett, D.D. et al. The impact of the human thalamus on brain-wide information processing. Nat Rev Neurosci 24, 416–430 (2023). https://doi.org/10.1038/s41583-023-00701-0

114) Nersisyan S, Bekisz M, Kublik E, Granseth B, Wróbel A. Cholinergic and Noradrenergic Modulation of Corticothalamic Synaptic Input From Layer 6 to the Posteromedial Thalamic Nucleus in the Rat. Front Neural Circuits. 2021;15:624381. Published 2021 Apr 26. doi:10.3389/fncir.2021.624381

115) Lytton WW, Destexhe A, Sejnowski TJ. Control of slow oscillations in the thalamocortical neuron: a computer model. Neuroscience. 1996;70(3):673-684. doi:10.1016/s0306-4522(96)83006-5

116) Kim J, Kim Y, Nakajima R, et al. Inhibitory Basal Ganglia Inputs Induce Excitatory Motor Signals in the Thalamus. Neuron. 2017;95(5):1181-1196.e8. doi:10.1016/j.neuron.2017.08.028

117) Magill PJ, Bolam JP, Bevan MD. Relationship of activity in the subthalamic nucleus-globus pallidus network to cortical electroencephalogram. J Neurosci. 2000;20(2):820-833. doi:10.1523/JNEUROSCI.20-02-00820.2000

118) Shine JM. Adaptively navigating affordance landscapes: How interactions between the superior colliculus and thalamus coordinate complex, adaptive behaviour. Neurosci Biobehav Rev. 2022;143:104921. doi:10.1016/j.neubiorev.2022.104921

119) Hwang K, Bruss J, Tranel D, Boes AD. Network Localization of Executive Function Deficits in Patients with Focal Thalamic Lesions. J Cogn Neurosci. 2020;32(12):2303-2319. doi:10.1162/jocn_a_01628

120) Snow JC, Allen HA, Rafal RD, Humphreys GW. Impaired attentional selection following lesions to human pulvinar: evidence for homology between human and monkey. Proc Natl Acad Sci U S A. 2009;106(10):4054-4059. doi:10.1073/pnas.0810086106

121) Herrero MT, Barcia C, Navarro JM. Functional anatomy of thalamus and basal ganglia. Childs Nerv Syst. 2002;18(8):386-404. doi:10.1007/s00381-002-0604-1

122) Xiong Y, Ye C, Chen Y, et al. Altered Functional Connectivity of Basal Ganglia in Mild Cognitive Impairment and Alzheimer's Disease. Brain Sci. 2022;12(11):1555. Published 2022 Nov 15. doi:10.3390/brainsci12111555

123) Botzung, A., Philippi, N., Noblet, V. et al. Pay attention to the basal ganglia: a volumetric study in early dementia with Lewy bodies. Alz Res Therapy 11, 108 (2019). https://doi.org/10.1186/s13195-019-0568-y

124) Xiong Y, Ye C, Chen Y, et al. Altered Functional Connectivity of Basal Ganglia in Mild Cognitive Impairment and Alzheimer's Disease. Brain Sci. 2022;12(11):1555. Published 2022 Nov 15. doi:10.3390/brainsci12111555

125) Wessel, J., Jenkinson, N., Brittain, JS. et al. Surprise disrupts cognition via a fronto-basal ganglia suppressive mechanism. Nat Commun 7, 11195 (2016). https://doi.org/10.1038/ncomms11195

126) Chen P, Ye E, Jin X, Zhu Y, Wang L. Association between Thalamocortical Functional Connectivity Abnormalities and Cognitive Deficits in Schizophrenia. Sci Rep. 2019;9(1):2952. Published 2019 Feb 27. doi:10.1038/s41598-019-39367-z

127) Cao, H., Chén, O.Y., Chung, Y. et al. Cerebello-thalamo-cortical hyperconnectivity as a state-independent functional neural signature for psychosis prediction and characterization. Nat Commun 9, 3836 (2018). https://doi.org/10.1038/s41467-018-06350-7

128) Braak H, Alafuzoff I, Arzberger T, Kretzschmar H, Del Tredici K. Staging of Alzheimer disease-associated neurofibrillary pathology using paraffin sections and immunocytochemistry. Acta Neuropathol. 2006;112(4):389-404. doi:10.1007/s00401-006-0127-z

129) Wang R, Dineley KT, Sweatt JD, Zheng H. Presenilin 1 familial Alzheimer's disease mutation leads to defective associative learning and impaired adult neurogenesis. Neuroscience. 2004;126(2):305-312. doi:10.1016/j.neuroscience.2004.03.048

130) Jack CR Jr, Petersen RC, Xu YC, et al. Prediction of AD with MRI-based hippocampal volume in mild cognitive impairment. Neurology. 1999;52(7):1397-1403. doi:10.1212/wnl.52.7.1397

131) Jayaraman, A., Htike, T.T., James, R. et al. TNF-mediated neuroinflammation is linked to neuronal necroptosis in Alzheimer's disease hippocampus. acta neuropathol commun 9, 159 (2021). https://doi.org/10.1186/s40478-021-01264-w

132) Cai L, Wei X, Liu J, et al. Functional Integration and Segregation in Multiplex Brain Networks for Alzheimer's Disease. Front Neurosci. 2020;14:51. Published 2020 Feb 18. doi:10.3389/fnins.2020.00051

133) Crowell CA, Davis SW, Beynel L, et al. Older adults benefit from more widespread brain network integration during working memory. Neuroimage. 2020;218:116959. doi:10.1016/j.neuroimage.2020.116959

134) Varangis E, Habeck CG, Razlighi QR, Stern Y. The Effect of Aging on Resting State Connectivity of Predefined Networks in the Brain. Front Aging Neurosci. 2019;11:234. Published 2019 Sep 4. doi:10.3389/fnagi.2019.00234

135) Ji L, Pearlson GD, Hawkins KA, Steffens DC, Guo H, Wang L. A New Measure for Neural Compensation Is Positively Correlated With Working Memory and Gait Speed. Front Aging Neurosci. 2018;10:71. Published 2018 Mar 19. doi:10.3389/fnagi.2018.00071

136) Larivière S, Xifra-Porxas A, Kassinopoulos M, et al. Functional and effective reorganization of the aging brain during unimanual and bimanual hand movements. Hum Brain Mapp. 2019;40(10):3027-3040. doi:10.1002/hbm.24578

137) Kwon, H.S., Koh, SH. Neuroinflammation in neurodegenerative disorders: the roles of microglia and astrocytes. Transl Neurodegener 9, 42 (2020). https://doi.org/10.1186/s40035-020-00221-2

138) Akiyama H, Barger S, Barnum S, et al. Inflammation and Alzheimer's disease. Neurobiol Aging. 2000;21(3):383-421. doi:10.1016/s0197-4580(00)00124-x

139) Liu C, Cui G, Zhu M, Kang X, Guo H. Neuroinflammation in Alzheimer's disease: chemokines produced by astrocytes and chemokine receptors. Int J Clin Exp Pathol. 2014;7(12):8342-8355. Published 2014 Dec 1.

140) Heppner FL, Ransohoff RM, Becher B. Immune attack: the role of inflammation in Alzheimer disease. Nat Rev Neurosci. 2015;16(6):358-372. doi:10.1038/nrn3880

141) DeTure, M.A., Dickson, D.W. The neuropathological diagnosis of Alzheimer’s disease. Mol Neurodegeneration 14, 32 (2019). https://doi.org/10.1186/s13024-019-0333-5

142) Monif, M., Reid, C.A., Powell, K.L. et al. Interleukin-1β has trophic effects in microglia and its release is mediated by P2X7R pore. J Neuroinflammation 13, 173 (2016). https://doi.org/10.1186/s12974-016-0621-8

143) Zhang, K., Wang, H., Xu, M. et al. Role of MCP-1 and CCR2 in ethanol-induced neuroinflammation and neurodegeneration in the developing brain. J Neuroinflammation 15, 197 (2018). https://doi.org/10.1186/s12974-018-1241-2

144) Scahill RI, Schott JM, Stevens JM, Rossor MN, Fox NC. Mapping the evolution of regional atrophy in Alzheimer's disease: unbiased analysis of fluid-registered serial MRI. Proc Natl Acad Sci U S A. 2002;99(7):4703-4707. doi:10.1073/pnas.052587399

145) Thompson PM, Hayashi KM, de Zubicaray G, et al. Dynamics of gray matter loss in Alzheimer's disease. J Neurosci. 2003;23(3):994-1005. doi:10.1523/JNEUROSCI.23-03-00994.2003

146) Vann SD, Nelson AJ. The mammillary bodies and memory: more than a hippocampal relay. Prog Brain Res. 2015;219:163-185. doi:10.1016/bs.pbr.2015.03.006

147) Štillová K, Jurák P, Chládek J, et al. The Role of Anterior Nuclei of the Thalamus: A Subcortical Gate in Memory Processing: An Intracerebral Recording Study. PLoS One. 2015;10(11):e0140778. Published 2015 Nov 3. doi:10.1371/journal.pone.0140778

148) Ferbinteanu J. The Hippocampus and Dorsolateral Striatum Integrate Distinct Types of Memories through Time and Space, Respectively. J Neurosci. 2020;40(47):9055-9065. doi:10.1523/JNEUROSCI.1084-20.2020

149) Ferbinteanu J. Contributions of Hippocampus and Striatum to Memory-Guided Behavior Depend on Past Experience. J Neurosci. 2016;36(24):6459-6470. doi:10.1523/JNEUROSCI.0840-16.2016